



Separation Control by Plasma Actuators: Effects of Direct Momentum Injection and Vortex Generation

Federico Messanelli¹ · Edoardo Frigerio² · Elia Tescaroli³ · Marco Belan³ 

Received: 15 February 2019 / Accepted: 9 October 2019 / Published online: 30 November 2019
© Springer Nature B.V. 2019

Abstract

In this work, Dielectric Barrier Discharge actuators with triangular tips on their exposed electrodes are applied on a NACA 0015 airfoil and tested in the wind tunnel at an airspeed of 20 m/s ($Re = 330k$); the actuator set has been defined after previous laboratory studies. Steady and pulsed actuation are tested on all devices, including a straight DBD as reference. Force coefficients and electrical power are measured for every actuator, evaluating their performance in terms of aerodynamic coefficients changes with respect to the smooth airfoil and to the unpowered case, which is also characterized by means of surface visualizations. The influence of discharge length and tip spacing is studied by image processing techniques. The local field of motion is characterized by means of boundary layer velocity profiles, acquired with plasma off and on. Boundary layer thickness and momentum coefficients are determined at different spanwise locations for all the devices. The results are discussed evaluating the different impacts of streamwise momentum injection and vortex generation on the actuators performance, assuming these mechanisms as proper models for the data interpretation. In turn, this leads to outline possible design rules for this kind of DBD.

Keywords Separation control · Plasma actuators · Dielectric barrier discharge

1 Introduction

In the research field of flow control, the dielectric barrier discharge (DBD) actuators have been extensively studied in the last years, and many DBD actuators have reached the technology readiness level for possible applications in low speed aerodynamics. The performance of a classic surface DBD depends on electrical and geometrical parameters, such as waveform, frequency and amplitude of the applied voltage, electrodes gap, material and thickness of the dielectric [1, 2]. In particular, the shape of the exposed electrode can have

✉ Marco Belan
marco.belan@polimi.it

¹ F.M., Parma, Italy

² SimScale GmbH, Munich, Germany

³ Politecnico di Milano, Milano, Italy

a strong influence on the intensity and the direction of the induced ionic wind, exploiting different kinds of flow control. Different spanwise-periodic shapes, such as serpentine, square-wave [3, 4] and serrated edge [2, 5, 6] have been studied both numerically and in the laboratory. These configurations induce streamwise and transverse ionic wind at the same time, so they can energize a boundary layer in different ways, by direct streamwise acceleration and by creating a 3D flow in the near field that gives rise to streamwise vortex structures. In turn, these vortices mix the high-speed external flow with the slow wall flow [4, 7], delaying the boundary layer separation. These vortices can also be created by plasma vortex generators or PVG [7, 8], that are arrays of straight DBDs parallel to the mean flow direction; however a standard PVG is usually not designed to give direct streamwise acceleration to the flow.

In previous works the authors have studied the effects of triangular tips on the active electrodes of DBDs and corona actuators [9–12], both at the bench in still air and on airfoils in the wind tunnel. The electrodes under test, named multi-tip, have tips of different aspect ratios (length/width) and spacings, separated from each other or adjacent as in serrated edge geometries. For DBDs, this geometry is capable to create simultaneously streamwise jets aligned with the tips and pairs of counter rotating streamwise vortices in the regions between adjacent tips. The previous studies [12] about an actuated airfoil with progressive airspeeds U (5 to 15 m/s) and Reynolds numbers (83k to 255k) led to identify the best geometry for a given performance parameter, for instance the lift increase in early stall. However, the best electrode shape may depend on the freestream velocity of the tests [13], owing to the different extents of the two working principles, momentum injection and vortex generation. In fact, the streamwise momentum injection (tips effect) is directly related to the induced ionic wind u_i of few m/s, and is expected to scale unfavourably as the airspeed U grows, whereas the vortex generation should take advantage of the velocity gradient in the baseline boundary layer and is expected to be more promising at higher velocities, as described in literature [7, 8, 14].

The present work contains an investigation about these two principles, starting from new wind tunnel tests at 20 m/s ($Re = 330k$) that include forces and electric power measurements, as well as surface visualizations to understand the passive effects of the unpowered actuators. For the specific characterization of the properties depending on tips spacing, discharge length measurements have been performed. Finally, velocity measurements in the boundary layer have been carried out to characterize the local flow downstream of the actuators. Moreover, the DBDs are operated here both with steady and pulsed actuation, including in the study the effects of different pulse frequencies and duty cycles. In fact, in literature the pulsed actuation has shown to be very effective, but it was mainly investigated on straight DBDs [15–20]. The present experiment is focused on a set of four actuators, tested comparatively on the same airfoil in the wind tunnel with a straight DBD as reference. The tests are carried out with the same dielectric thickness, voltage and waveforms for the whole set, and the multi-tip electrodes share the same tip sharpness with different tip spacings.

The present results are discussed and interpreted accounting also for the outcome of previous experiments. Assuming to represent the physics by means of the two above mentioned working principles, they seem to have different impacts as function of the freestream velocity: it is proposed a physical interpretation where the direct momentum injection is more effective at low airspeeds, whereas the vortex generation improves at high airspeeds, provided that the geometry of the actuator satisfies suitable conditions, as exposed in the final discussion. The relevant scaling laws lead to hypothesize proper design rules for this kind of DBDs.

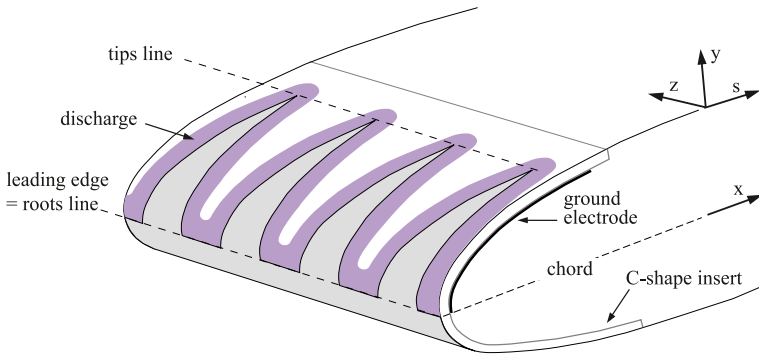


Fig. 1 Section of a DBD actuator: shape and alignment on the airfoil (GND electrode thickness enlarged for clarity)

2 Experiment Setup

2.1 DBD actuators

The actuators under test are assembled on C-shape PMMA inserts that fit accurately a corresponding cavity on the nose of a NACA 0015 profile, as shown in Fig. 1. The 2 mm-thick inserts are obtained by thermoforming PMMA sheets on a mold. Their shape is finished in such a way that the overall NACA 0015 profile is not changed when they are installed on the airfoil. The PMMA inserts work also as dielectric for the actuators, whose electrodes are made of aluminium tape, 0.12 mm thick in order to ensure a reliable duration to the sharp tips. The roots of the exposed electrode and the underlying edge of the ground electrode are always aligned with the leading edge line, in order to act on the early boundary layer, near or upstream of the separation point when possible.

In this work, 4 different multi-tip DBDs have been considered and compared to a straight DBD as a reference: 2 multi-tips have already been studied at the bench [9] and in the wind tunnel with steady actuation [12], whilst the remaining 2 have been purposely introduced for this experiment. With respect to the larger set of 15 DBDs studied in the previous works, the present selection stems from the outcome of preliminary tests at $U = 20$ m/s [13], since they indicate the geometries with long and sharp tips as favoured with increasing airspeeds and Reynolds numbers. The electrodes geometry is represented in flat form in Fig. 2: (a)

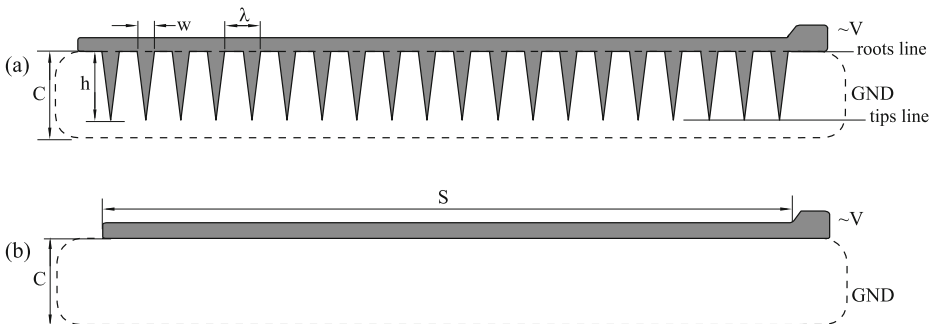


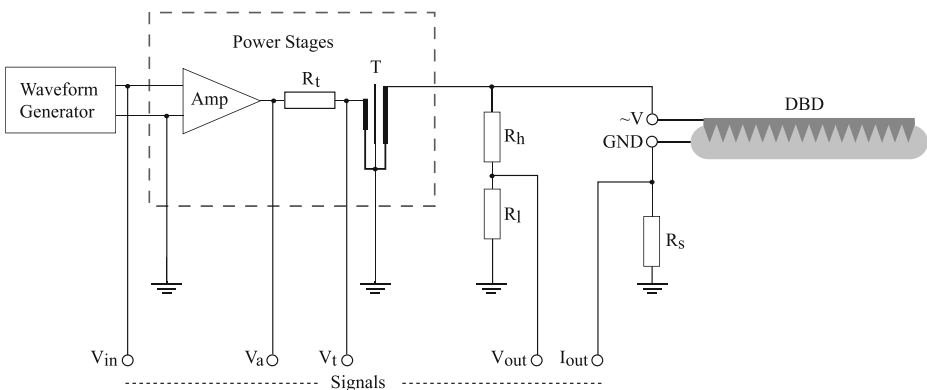
Fig. 2 Geometries of the 5 DBDs in flat form: **a** multi-tip D14, D15, D16, D17; **b** reference plate-to-plate D1

Table 1 DBD actuators under test

| Name | h , mm | w , mm | $n = N/S$, m^{-1} | $r = h/w$ | $\lambda = 1/n$, mm |
|------|----------|----------|----------------------|-----------|----------------------|
| D1 | 0 | – | – | 0 | – |
| D14 | 35 | 10 | 100.0 | 3.5 | 10 |
| D15 | 40 | 10 | 50.0 | 4 | 20 |
| D16 | 40 | 10 | 66.7 | 4 | 15 |
| D17 | 40 | 10 | 33.3 | 4 | 30 |

represents the multi-tip DBDs, both with non-adjacent tips (D15, D16, D17) and adjacent tips (D14), depending on their spacings λ ; (b) is the straight DBD used as reference and labeled D1. The specific geometry of each actuator is described in Table 1, that reports the length h and width w of the tips, the tips density $n = N/S$ (tips number per unit length), the sharpness $r = h/w$ and the inter-tip distance $\lambda = 1/n$ (spacing). The table is ordered by DBD name, including the new D16 and D17 in the last rows and maintaining the naming convention of the cited works. Excluding D1, the DBDs differ essentially in the tips spacing λ whilst the tip shape remains the same (D14 has slightly shorter tips for constructive reasons). All the actuators have a working span $S = 400$ mm so that more than 85% of the airfoil span is covered by the electrodes. The chordwise length of the ground electrode is always $C = 50$ mm, sufficient to allow for the complete development of the discharge.

The DBDs are driven by an oscillator+amplifier+transformer system capable of 100 W at $V_{pp} = 20$ kV, already described in the cited works [9, 12]. The electrical setup is shown in Fig. 3, including the measurement section, made of a 1:1000 voltage divider (R_h and R_l , load 47 M Ω) and a non-inductive shunt resistor ($R_s = 68$ or 100 Ω) connected to a 350 MHz oscilloscope with 20 Mrecords/trace. The accuracy of the power measurement system is improved in the present work by acquiring also the voltage and current waveforms on the primary winding of the power transformer (see V_a , V_t outputs in Fig. 3) and – accounting for the transformer efficiency and the circuit losses – comparing the relevant power to the one read at the actuator. The overall uncertainty on the electrical power, combining the effects of the various error sources in the electrical measurements, is ± 0.75 W.

**Fig. 3** Electrical setup for the DBD actuators

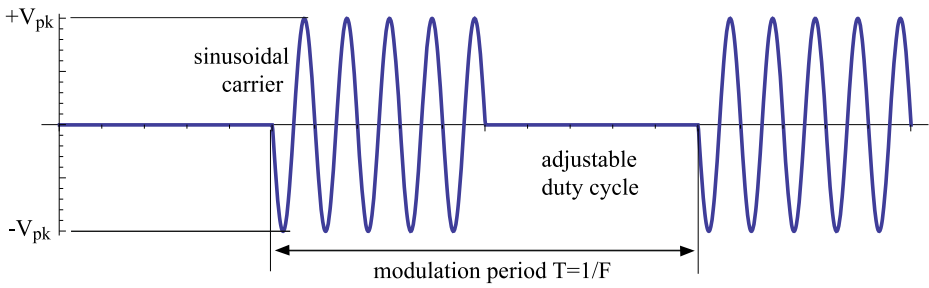


Fig. 4 Voltage waveform and principle of operation for pulsed DBDs

Steady and pulsed actuation are possible. For the latter, the well known principle of operation is sketched in Fig. 4: the voltage waveform to the actuator is a sinusoidal carrier set cyclically on and off by a modulation frequency. The carrier frequency, tuned to minimize the power losses under steady conditions [21], is $f = 800$ Hz for actuator D1, and $f = 640$ Hz for D14 to D17. The modulation frequency F , as usual, is more conveniently expressed in dimensionless form as a reduced frequency $F_+ = Fc/U$, scaled on the airfoil chord and the freestream velocity. In the modulation period $T = 1/F$, the active time is adjustable by setting the duty cycle D_c , and in force measurements the performance of each actuator is evaluated as function of both the parameters F_+ and D_c .

During the active phase, after a short transient the voltage and current waveforms take substantially the same trends as for steady operation. An example of such curves recorded along a carrier period at the beginning of a wave train (active phase) is shown in Fig. 5 for the actuator D17. The voltage amplitude, in this example and in all the aerodynamic tests, is always $V_{pp} = 20 \pm 0.2$ kV, in order to study the effects of the electrode shapes while keeping the same voltage and waveforms. With the same voltage at the bench and steady actuation, the 4 multi-tips induce a maximum ionic wind u_i in the range 2.45 to 2.65 m/s (tips aligned) whilst the straight D1 gives 1.80 m/s.

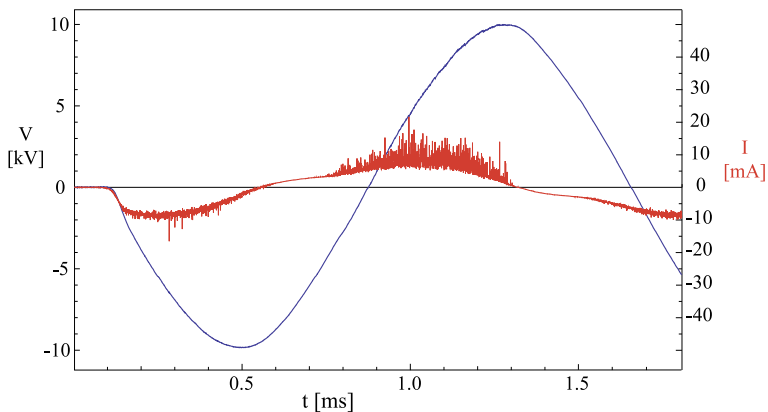


Fig. 5 Voltage and current of the DBD D17 along the 1st carrier period of an active phase

2.2 Wind tunnel, airfoil and balance

The experiment has been carried out in an open-circuit wind tunnel in the aerodynamic laboratory of the Aerospace Department (DAER) of Politecnico di Milano, already described in [11, 12]. A sketch of the setup is presented in Fig. 6. The test section is $0.5 \times 0.7 \text{ m}^2$ in cross section and 2 m in length. The maximum velocity is 25 m/s and the maximum turbulence level is 0.5%. The airfoil is a NACA 0015 of chord $c = 0.25 \text{ m}$ and span $b = 0.47 \text{ m}$, already used and described in [11, 12]. End plates made in PMMA are located at the two lateral edges of the airfoil, in order to limit end effects and partially recover 2D behaviour. The angle of attack α is set by means of a positioning system of optical quality (accuracy $\pm 0.005^\circ$), and its overall uncertainty, accounting for the residual crossflow in the test section, is better than $\pm 0.1^\circ$. All the actuators have been tested at 20 m/s, corresponding to a nominal Reynolds number of 330k based on the chord length. Some actuators in few special tests have been tested also at 22.5 m/s.

The airfoil is connected to the external aerodynamic balance by two lateral trunnions. The balance is made of 4 load cells, symmetrically located on the two sides of the test chamber. Two cells are sensitive to horizontal loads (range 50 N, accuracy of $\pm 0.01 \text{ N}$), the other two are sensitive in the vertical direction (range 100 N, accuracy $\pm 0.02 \text{ N}$). Lift and drag curves have been acquired for increasing values of α in the range $0^\circ \leq \alpha \leq 35^\circ$; in each measurement, the angle of attack was always set first to 0° and then taken to the desired value, in order to prevent hysteresis effects. The analog signals of loads have been

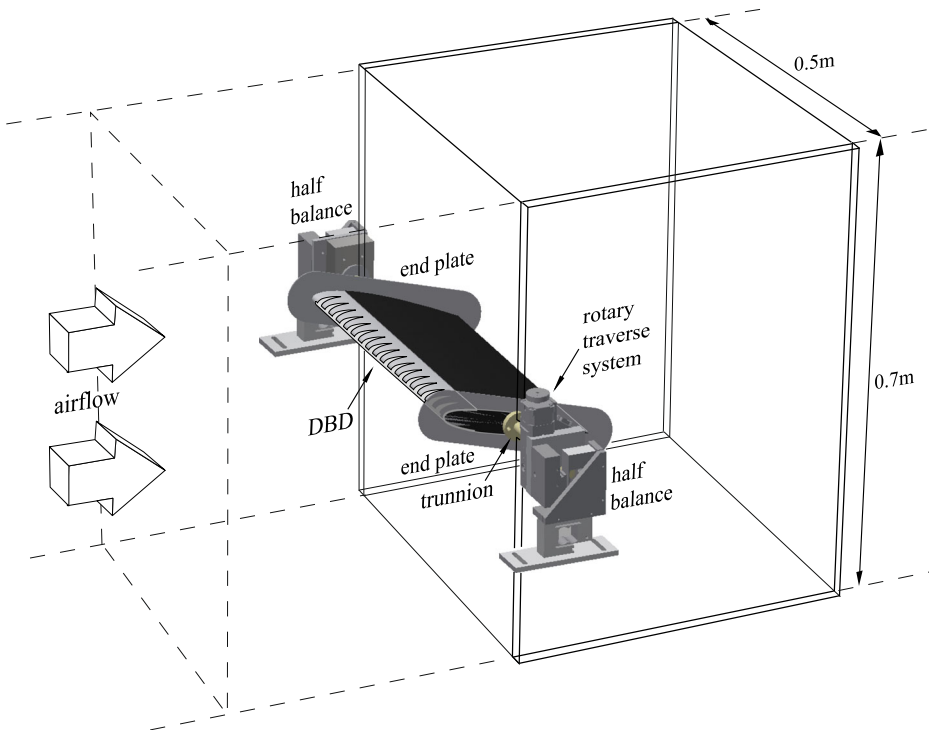


Fig. 6 Experimental setup: airfoil, balance and parts of the tunnel walls. Interchangeable panels permit visualizations and access for pressure probes

acquired and digitally converted at 4 kSamples/s with 16 bit depth. Each single datum is obtained as a time average over at least 10 s. In terms of standard deviations, the resulting overall uncertainties on the force coefficients c_l and c_d at $U = 20$ m/s are $(\sigma_{c_l}, \sigma_{c_d}) = (0.0061, 0.0027)$. These values represent the worst operating conditions, corresponding to the stalled airfoil, whilst for small α the values of σ_{c_l} and σ_{c_d} are lower. The uncertainties of force coefficients are particularly important in quantifying the plasma discharge effect, i.e. when measuring the force variations generated by switching on the actuators. At stall inception for high airspeeds, these variations can be small and to ensure reliable results this kind of measurements has been repeated numerous times under the same conditions, in order to determine mean values and uncertainties. For example, this procedure has been followed for the ratio $(c_{l,on} - c_{l,off})/c_{l,off}$ which represents a normalized variation due to the discharge effect: the range $14.2^\circ \leq \alpha \leq 15.8^\circ$ around the critical (stall inception) value has been scanned with 0.1° step, and for each α value $c_{l,on}$ and $c_{l,off}$ have been acquired as 10 s average measurements automatically repeated 100 times, evaluating then mean value and standard deviation for $(c_{l,on} - c_{l,off})/c_{l,off}$. In the results section (Section 3.3) and in the discussion (Section 4), the final data and their uncertainties have been determined by means of these procedures.

Corrections for confined flows have been implemented following the analysis presented in [22]. In particular, solid and wake blockage corrections have been taken into account:

$$\epsilon_b = \epsilon_{sb} + \epsilon_{wb} = \Lambda \sigma_b + \frac{c/H}{2} c_{du} \tag{1}$$

where H is the height of the test section, c_{du} is the uncorrected drag coefficient, $\Lambda = 0.3$ is the body shape factor for the thickness ratio of the present airfoil and

$$\sigma_b = \frac{\pi^2}{48} \left(\frac{c}{H}\right)^2. \tag{2}$$

The resulting corrected quantities are:

$$U = U_u(1 + \epsilon_b) \tag{3}$$

$$c_l = c_{lu}(1 - \sigma_b - 2\epsilon_b) \tag{4}$$

$$\alpha = \alpha_u + \frac{90 \sigma_b}{\pi^2} c_{lu} \tag{5}$$

$$c_d = c_{du}(1 - 3\epsilon_{sb} - 2\epsilon_{wb}). \tag{6}$$

Here the uncorrected values are labeled by the subscript u . In the results section, all the data are directly presented in corrected form (for high blockages, the effective Reynolds number increases by a factor 1.03).

2.3 Other diagnostics

With the aim of understanding the passive effects of the actuators and delineate the boundary layer of the baseline flow, surface visualizations have been performed on the airfoil in the wind tunnel, with different configurations. The china clay technique has been chosen, because it permits an easier cleaning of model and actuators, with respect to other dif-fused techniques. These visualizations are realized by accessing the test section from above, with the airfoil set to positive angles of attack. To increase the image contrast, the surface of the model is matt black painted. After each test, images of the model surface have been acquired. In order to retrieve the desired flow details, the original image resolution is 5568×3712 and the depth is 24 bit.

In order to investigate the effects of tip spacing, the plasma region extent has been separately studied at the bench. The discharge length has been determined along a direction locally normal to the electrode contour by means of the image processing method introduced by Kriegseis et al. [23], recalled in detail in Section 3.4. To acquire these images, a setup with good sensitivity has been used, with resolution 1300×1030 , depth 12 bit and long exposures, up to 4 s.

The characterization of the local boundary layer, both with plasma off and on, is performed through velocity measurements acquired downstream of the actuators. A total pressure probe, with outer diameter $d_p = 0.4$ mm, has been traversed over the model, keeping it parallel to the local tangent of the airfoil surface. The traversing system has a vertical and a spanwise degree of freedom and is mechanically decoupled from the test section frame, in order to improve the positioning accuracy. The pressure values are acquired by transducers with range 254 Pa or 1270 Pa and accuracy $\pm 0.1\%$. Corrections for the wall and shear effects are applied where necessary. The resulting uncertainty of the velocity measurements is in the order of $\pm 1.5\%$, excepting the points lying at less than $2d_p$ from the wall, where the uncertainty can worsen to $\pm 18\%$: in this region, not repeatable measurements have been discarded.

3 Results

3.1 Baseline flow and passive effects of the electrodes

In Section 3.3, the effectiveness of the DBDs will be reported in terms of variations of lift and drag by comparing the performance with plasma off and on, even with respect to the bare airfoil. In fact, also the unpowered actuators produce a non-negligible effect on the airfoil aerodynamics [24], and this point is treated in the present section in order to give a complete description of the phenomenon under study. The baseline flow is reproduced here by means of a C insert without electrodes, and the relevant lift and drag curves vs. α are acquired and used as reference data. These data are strictly valid only with the present setup, because the flow around the airfoil is not ideally two-dimensional and depends on the setup itself. Indeed, different data can be found in literature for the NACA 0015: for example, the spreading of maximum lift coefficients reported for this airfoil in different experiments on the narrow interval $220k \leq Re \leq 260k$ ranges from $c_{lM} = 0.95$ to more than 1.2, depending on the different aspect ratios, end or splitter plates used in each work [19, 25–27].

All the actuators in this work do not change the lift coefficient at small angles of attack, whereas their effect becomes significant when α is close to the critical value α_c (stall inception). At the present Reynolds number the original boundary layer on the smooth profile is laminar at the leading edge, then downstream of a recirculation bubble and an unsteady reattachment, the transition to turbulence takes place. As the angle of attack increases, the laminar zone shortens, and for $\alpha \sim \alpha_c$ the bubble reattaches approximately at $15 \text{ mm} = 0.06c$ from the leading edge, whilst downstream of this zone the transition to turbulence swiftly takes place. This behaviour can be described with numeric tools as XFOil [28] or visualized as in Fig. 7, that depicts the baseline boundary layer state for $\alpha = 13.5^\circ$. In detail, on the leading edge zone the short streaks aligned with the incoming flow indicate a laminar region, then the heavy accumulation of color marks the position of the recirculating bubble. The following region, weakly colored, corresponds to the unsteady reattachment zone, where the end of the bubble moves back and forth, and finally the small structures on the following region depict a fast transition to a turbulent boundary layer.

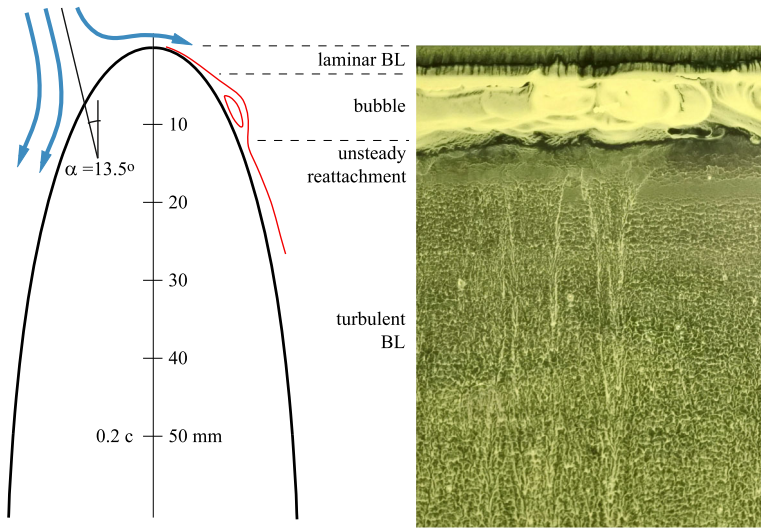


Fig. 7 Baseline flow: surface visualization of the suction side of NACA0015 at mid-span, for $\alpha = 13.5^\circ$ at $U = 20 \text{ m/s}$ or $Re = 330k$. In the left side sketch (red lines), the BL thickness is enlarged for clarity

In general, the unpowered actuators on the airfoil surface can give measurable effects, since the 0.12 mm thickness of the electrodes is not negligible on the boundary layer scale in that zone (the relevant measurements are reported in Section 3.5). The tips are in the sensitive region where the transition takes place, thus the lift coefficient of the airfoil with different actuators is quite scattered in the post-critical region. Figure 8 shows the $c_{l,off}(\alpha)$ curves for the DBD set under test, including the baseline airfoil with the smooth insert. In the critical range $\alpha \sim \alpha_c$, only for the straight DBD D1 the changes in lift curve are small, as was noticed also in other experiments [27]. All the multi-tips instead delay the stall and give a small increase of the maximum lift coefficient, i.e. $c_{lM,off} > c_{lM}$. This is due to a faster transition to turbulence, promoted by the electrodes shape. In detail, the original flow

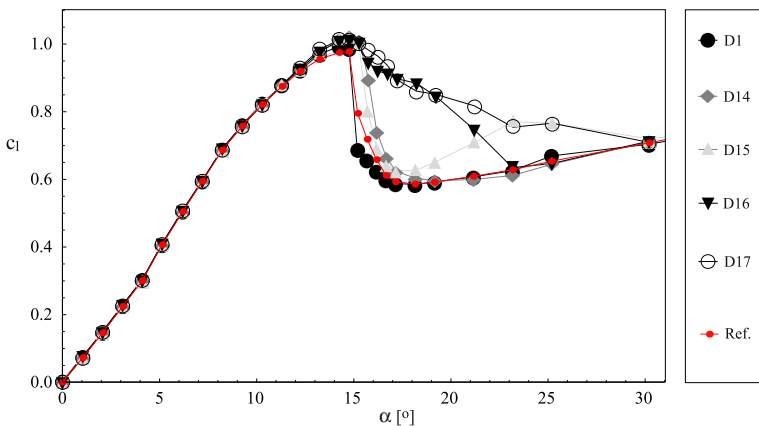


Fig. 8 $c_{l,off}(\alpha)$ curves at $U = 20 \text{ m/s}$, compared with the reference $c_l(\alpha)$ without electrodes

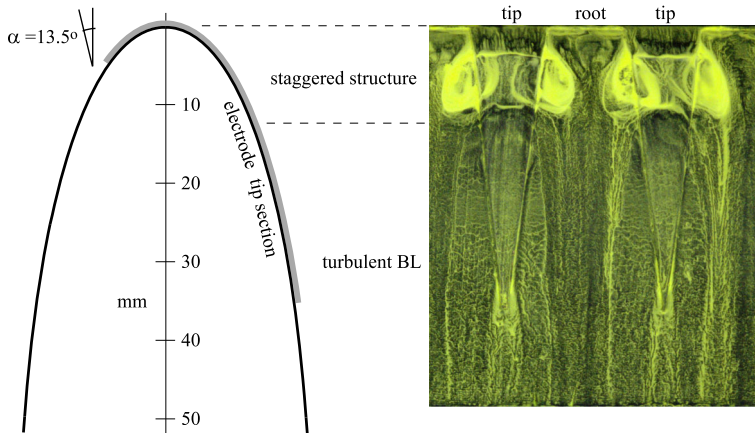


Fig. 9 Surface visualization on the DBD D15, mid-span, $\alpha = 13.5^\circ$, $U = 20$ m/s (electrode thickness not to scale)

is manipulated by the unpowered electrode giving rise to a staggered flow pattern, as shown in Fig. 9: the laminar streamwise flow survives for few millimeters over the tips only, whilst in the inter-tip spaces very small bubbles can be observed. The original bubble is modified to a spanwise-periodic sequence of vortex structures, and the overall effect is a more rapid transition along the chordwise direction. The flow pattern of Fig. 9 represents effectively the whole set of multi-tips, including the adjacent tips of D14: in that case, also the vortex structures between tips become adjacent and move closer to the leading edge.

As regards the postcritical range, in Fig. 8 the actuators D1 and D14 give a lift drop similar to the reference, whilst D16 and D17 create a large and slow stall delay; moreover, D15 gives rise also to a secondary lift peak. These effects have been checked and confirmed even by building some copies of the original actuators on new C-shape inserts, installing them on the airfoil and repeating the tests. In deep stall the flow structures in the separated region are presumably different for each electrode shape, and a detailed interpretation can not be obtained exclusively by means of surface visualizations, however these behaviours suggest to consider the unpowered multi-tips as weak vortex generators of very low profile [29]. The tip spacing has an important role in determining their lift curves, including the secondary peak already observed in the relevant literature [30]. The discharge operates on a flow already influenced by the electrodes shape, therefore the following results will be presented in such a way as to retain the information about the passive effects as far as possible.

3.2 Performance parameters

As regards the aerodynamic forces, the actuators performance can be assessed in two ways: I) focusing on the relative variations (plasma off vs plasma on) occurring with a certain actuator. This variation, $(c_{l,off}, c_{d,off})$ to $(c_{l,on}, c_{d,on})$, arises exclusively from the discharge effect and is widely reported in literature; II) considering the total variations between the smooth airfoil of coefficients (c_l, c_d) and the actuated airfoil (with a powered DBD) of coefficients $(c_{l,on}, c_{d,on})$, that permits to include and evaluate the passive effects of the electrodes. The two measurable variations are sketched in Fig. 10 for the lift coefficient curves.

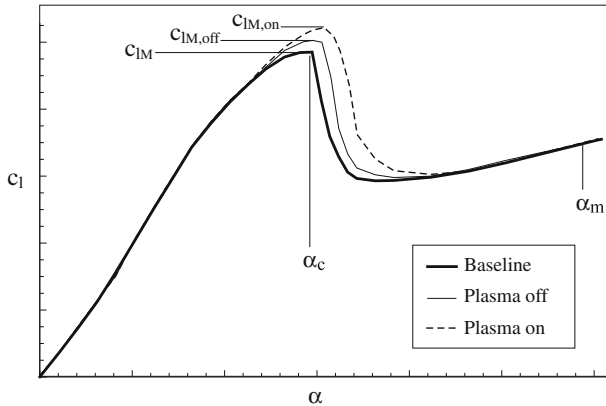


Fig. 10 Progressive variations of the lift coefficient: thick line = baseline c_l curve, smooth airfoil; thin line = $c_{l,off}$ curve, airfoil with unpowered actuator; dashed line = $c_{l,on}$ curve, airfoil with plasma on

The approaches I) and II) lead to define different parameters, as explained in what follows. A first parameter is defined by the normalized lift increase at critical point, as in [11, 12]: according to the two approaches I) and II), the relative variation (plasma off to plasma on) is

$$\Delta c_{lMp} = \frac{c_{lM,on} - c_{lM,off}}{c_{lM,off}} \tag{7}$$

whilst the total variation (baseline to plasma on) is

$$\Delta c_{lMt} = \frac{c_{lM,on} - c_{lM}}{c_{lM}}. \tag{8}$$

These parameters will be expressed in percentage form. They are related to specific values of α (the critical points), hence they can be considered local parameters. The actuators can also be characterized by introducing global parameters, related to the overall variation of lift and drag curves as follows. With regard to the off–on variation (I), the mean lift increase can be defined as

$$\langle \Delta c_l \rangle_p = \frac{\int_0^{\alpha_m} (c_{l,on} - c_{l,off}) d\alpha}{\int_0^{\alpha_m} c_{l,off} d\alpha} \tag{9}$$

whilst the total variation (baseline to on, II) is expressed by

$$\langle \Delta c_l \rangle_t = \frac{\int_0^{\alpha_m} (c_{l,on} - c_l) d\alpha}{\int_0^{\alpha_m} c_l d\alpha}. \tag{10}$$

In a similar way, the mean drag reduction for the plasma (I) and total variation (II) are respectively

$$\langle \Delta c_d \rangle_p = \frac{\int_0^{\alpha_m} (c_{d,off} - c_{d,on}) d\alpha}{\int_0^{\alpha_m} c_{d,off} d\alpha}; \quad \langle \Delta c_d \rangle_t = \frac{\int_0^{\alpha_m} (c_d - c_{d,on}) d\alpha}{\int_0^{\alpha_m} c_d d\alpha}. \tag{11}$$

All the above integrals are computed over the same range $0 \leq \alpha \leq \alpha_m$. As shown in Fig. 10, the main contribution to these parameters is due to the gap between curve pairs (base–on or off–on) in the postcritical range, and the integral values become independent of α_m when this limit is sufficiently large, where the difference between the curves is negligible within the uncertainty level; in order to acquire robust results, the parameters previously defined

are evaluated here over the interval $0 \leq \alpha \leq 35^\circ$. The above parameters are calculated on interpolated data, according to the method described in [11]. In particular, this is helpful in minimizing the errors on the local parameters Δc_{lM_i} and Δc_{lM_p} , that are more sensitive to local random variations of the data points. In what follows, the actuators will be mainly compared on the basis of plasma effect, focusing on Δc_{lM_p} for early stall and $\langle \Delta c_l \rangle_p$ for deep stall; the corresponding total parameters Δc_{lM_t} and $\langle \Delta c_l \rangle_t$ will be reported to improve the comprehension of the passive effects, keeping in mind that the global parameter $\langle \Delta c_l \rangle_t$ collects the different and complicated passive behaviours of the treated DBDs in integral values.

Another field of comparison arises by considering the effectiveness in terms of power: here the DBDs can be compared by means of two parameters already introduced in [11]: the critical lift effectiveness

$$\varepsilon_{lcp} = \frac{\Delta L_{Mp}}{W_c} = \frac{L_{M,on} - L_{M,off}}{W_c}, \tag{12}$$

where $L_{M,on} - L_{M,off}$ is the difference in maximum lift due to plasma discharge and W_c the relevant power consumption at stall inception; and the mean lift effectiveness

$$\varepsilon_{lmp} = \left\langle \frac{\Delta L_p}{W_e} \right\rangle = \int_0^{\alpha_m} \frac{L_{on} - L_{off}}{W_e} d\alpha, \tag{13}$$

which is the mean ratio of plasma lift increase to electric power consumption. Here the average electric power consumption is obtained by means of the electrical setup of Fig. 3 and according to the procedure described in Section 2.1 as

$$W_e = \frac{1}{T} \int_0^T V(t)I(t) dt, \tag{14}$$

where T is a finite number of cycles. ε_{lcp} , ε_{lmp} are parameters of kind (I) based on the plasma effect; in a similar way, the corresponding parameters for the total variation (II), namely ε_{lct} , ε_{lmt} , can be easily defined. The above quantities have dimensions of N/W, but they can be brought to dimensionless form by referring to a possible flight test where the same airfoil lifts a load with vertical velocity U_y and mechanical power $U_y L$. For instance, the parameters ε_{lcp} and ε_{lmp} lead then to the power saving ratios

$$\eta_{lcp} = U_y \Delta L_{Mp} / W_c \tag{15}$$

$$\eta_{lmp} = (U_y / \alpha_m) \langle \Delta L_p / W_e \rangle. \tag{16}$$

In possible real flight applications, values greater than 1 for these parameters would mean that a certain electrical power controls a larger mechanical power.

For every actuator, all the performance parameters can be acquired with different electrical settings, by changing modulation frequency F_+ and duty cycle D_c for each test. This leads to a large amount of data that will be presented in the next sections, by remarking the most meaningful results. The criterion adopted to explore the parameter space F_+, D_c is delineated in what follows: considering the existing literature and the results of preliminary measurements, the test grid (Fig. 11) is mainly focused on a low frequency $F_+ = 1$, a high $F_+ = 4$, and on two duty cycles $D_c = 0.2$ and 0.5 ; the map is then completed with other values of (F_+, D_c) , by the top line (steady actuation) and by the bottom line (actuator off). For each point (F_+, D_c) , the force coefficients as functions of α are acquired, leading to 40 tests for each actuator. For high F_+ and low D_c the pulse duration can also be shorter than the carrier period: these points lie below the line $D_c = F/f$, shown in figure for $f = 800$ Hz.

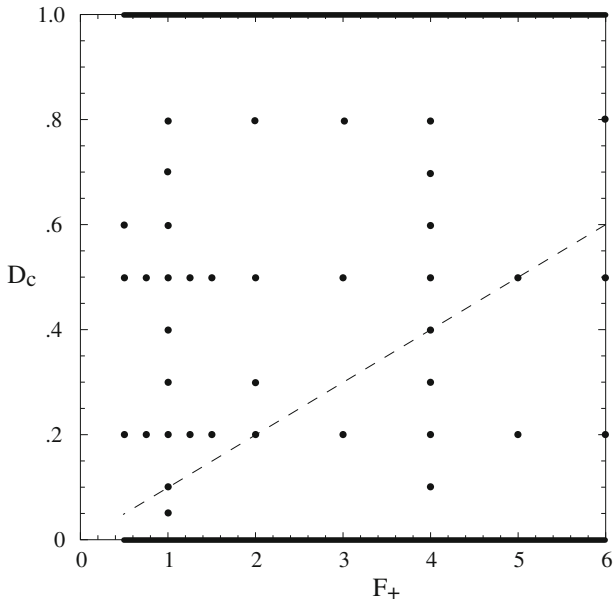


Fig. 11 Space parameter exploration: black points and thick lines are tested for all actuators (top line = steady actuation; bottom line = no actuation). Below the dashed line the pulse duration is shorter than the carrier period of 1/800 s

3.3 Force measurements

The performance of the actuators in increasing the maximum lift is presented in Table 2, where the actuators are listed in descending order of relative (plasma off-on) increase Δc_{lMp} . Next to the Δc_{lMp} column, the table reports the total increase Δc_{lMt} (baseline to plasma on), together with the working conditions (F_+ , D_c) for which those maxima are measured (optimal performance with steady actuation is indicated by $D_c = 1.0$). The uncertainty of Δc_{lMp} and Δc_{lMt} is in the order of $\pm 0.7\%$. Each row is completed by the electrical data, namely the power consumption per unit length W_e/S , the power to active perimeter ratio W_e/l , and the relative and total critical lift effectiveness ϵ_{lcp} , ϵ_{lct} defined above. The

Table 2 Stall inception performance at $U = 20$ m/s

| Act. | Δc_{lMp} , % | Δc_{lMt} , % | F_+ | D_c | W_e/S , W/m | W_e/l , W/m | ϵ_{lcp} , N/W | ϵ_{lct} , N/W |
|------|----------------------|----------------------|-------|-------|---------------|---------------|------------------------|------------------------|
| D17 | 3.4 | 7.2 | | 1.0 | 41.2 | 11.9 | 0.063 | 0.13 |
| D15 | 3.4 | 7.0 | | 1.0 | 44.8 | 9.9 | 0.055 | 0.11 |
| D1 | 2.3 | 4.0 | 4.0 | 0.8 | 10.1 | 10.1 | 0.167 | 0.29 |
| D14 | 2.2 | 6.7 | 4.0 | 0.8 | 27.0 | 3.8 | 0.059 | 0.18 |
| D16 | 1.8 | 5.3 | 4.0 | 0.8 | 35.8 | 6.2 | 0.039 | 0.11 |

Best values of maximum lift increases (off-on and total), with working conditions, power and effectiveness parameters

active perimeter l is the length of the electrode contour along the tips side, i.e. the effective plasma generating length, so the W_e/l ratio adds information about the specific power consumption as function of the geometry.

Table 2 reveals that the highest lift increases at the critical angle of attack α_c are obtained with steady actuation or in the worst cases with high duty cycles, thus the pulsed actuation is not much effective on this parameter (this has been also evidenced in literature [18, 31]). On the other hand, the pulsed actuation works better in the postcritical range of α , as will be shown below. In particular, in Table 2 the best Δc_{lMp} is given by D17 along with D15: in Sections 3.4 and 4 it will be shown that the key parameter is in this case their large inter-tip spacing λ , that allows them to work as effective VG.

Besides the effects on the flow, it is clear that different geometries imply different active perimeters l and power consumptions W_e , and it is worth to observe that the devices with high lift increase Δc_{lMp} have also high W_e/l ratios for the same supply voltage. Finally, it is noticeable that in these tests, even if the multi-tips with large spacings λ perform better than D1, the straight actuator maintains a large effectiveness in N/W. This is related to the short active length $l = S$ of D1, whilst for multi-tips the active perimeter l can be much larger than S , potentially leading to larger power consumptions.

The quantitative data of Table 2 come from a large set that is more easily visualized in graphical form. For the three best actuators (D17, D15 and D1), the Δc_{lMp} maps as functions of F_+ , D_c can be seen in Fig. 12. Here the measured quantity is shown by means of interpolated surfaces over the (F_+, D_c) domain, in order to reveal the main trends of lift increase: for the early stall parameter Δc_{lMp} it is evident that steady actuation ($D_c = 1$) is the best choice, and even for D1, where the maximum is located in $(F_+, D_c) = (4, 0.8)$, the line $D_c = 1$ represents a high performance region. Examples of specific lift curves can be seen in Fig. 14, which is reported later to include the pulsed actuation results.

Table 2 reports also the total lift increases Δc_{lMt} with respect to the baseline or smooth airfoil: these are larger than plasma contributions Δc_{lMp} , owing to the passive effects discussed in Section 3.1. In general, all the electrodes act on the early boundary layer increasing the unsteadiness and promoting a faster transition; this effect is relatively larger for D14 and D16, where the passive effect of their numerous tips is coupled with weaker plasma contributions. It is not necessary to plot the corresponding maps for the total effect $\Delta c_{lMt}(F_+, D_c)$, since they have shapes similar to the ones in Fig. 12: in fact, their data points are linearly dependent from the Δc_{lMp} , and it is simple to prove from the definitions (7) and (8) that

$$\Delta c_{lMt}(F_+, D_c) = A \Delta c_{lMp}(F_+, D_c) + B, \tag{17}$$

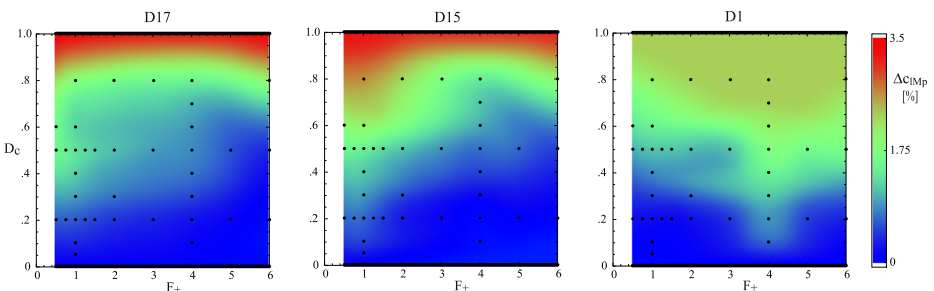


Fig. 12 Maps of Δc_{lMp} as function of F_+ and D_c for D17, D15 and D1 at $U = 20$ m/s

Table 3 Deep stall performance at $U = 20$ m/s

| Act. | $\langle \Delta c_l \rangle_p$, % | $\langle \Delta c_l \rangle_t$, % | F_+ | D_c | W_e/S , W/m | W_e/l , W/m | ε_{imp} , N/W | ε_{imt} , N/W |
|------|------------------------------------|------------------------------------|-------|-------|---------------|---------------|---------------------------|---------------------------|
| D1 | 23.8 | 23.7 | 1.0 | 0.1 | 1.4 | 1.4 | 11.40 | 11.35 |
| D15 | 18.3 | 28.8 | 1.0 | 0.1 | 4.5 | 1.0 | 2.74 | 4.33 |
| D14 | 5.1 | 9.0 | 4.0 | 0.8 | 27.0 | 3.8 | 0.13 | 0.23 |
| D17 | 3.4 | 23.8 | 0.5 | 0.5 | 20.6 | 5.9 | 0.12 | 0.80 |
| D16 | 3.8 | 21.1 | 4.0 | 0.8 | 35.8 | 6.2 | 0.07 | 0.41 |

Best mean lift increases (on-off and total), working conditions and electric parameters

where A and B are constants, specific of each actuator and independent of F_+ and D_c . In general, each total parameter (base to plasma on) is related to the corresponding discharge effect parameter (plasma off to on) by this property.

To characterize the deep stall performance of the actuators, the integral parameter $\langle \Delta c_l \rangle_p$ is more useful because it depends primarily on the lift curve variation in the post-critical range of α . These data are presented in Table 3, where the actuators are listed in descending order of relative mean lift increase $\langle \Delta c_l \rangle_p$ (plasma off to on). The corresponding total mean lift increase $\langle \Delta c_l \rangle_t$ is shown in the next column, together with the relevant working conditions (F_+ , D_c), and followed by the electrical data W_e/S , W_e/l and the mean lift effectiveness ε_{imp} and ε_{imt} . The uncertainty of $\langle \Delta c_l \rangle_p$ and $\langle \Delta c_l \rangle_t$ is in the order of $\pm 0.7\%$.

In general, the data in Table 3 confirm that pulsed actuation is effective in deep stall control, in contrast to steady actuation which is more useful in increasing the maximum lift (Table 2). With respect to the data of Table 2 about early stall, here the performance of multi-tips drops, and only D15 maintains a good performance but it does not exceed D1. Both D1 and D15 work at best with short pulses and high power saving ($D_c = 0.1$) at modulation frequency $F_+ = 1$, and the highest effectiveness in N/W is achieved by D1, thanks to its small active length and power consumption. The passive effects of multi-tips, as before, give positive contributions to the lift increase so that $\langle \Delta c_l \rangle_t$ is larger than $\langle \Delta c_l \rangle_p$, particularly for D16 and D17 where passive effect is well larger than plasma effect. The passive contribution brings also D15 above D1 in the $\langle \Delta c_l \rangle_t$ column. The behaviour of D1

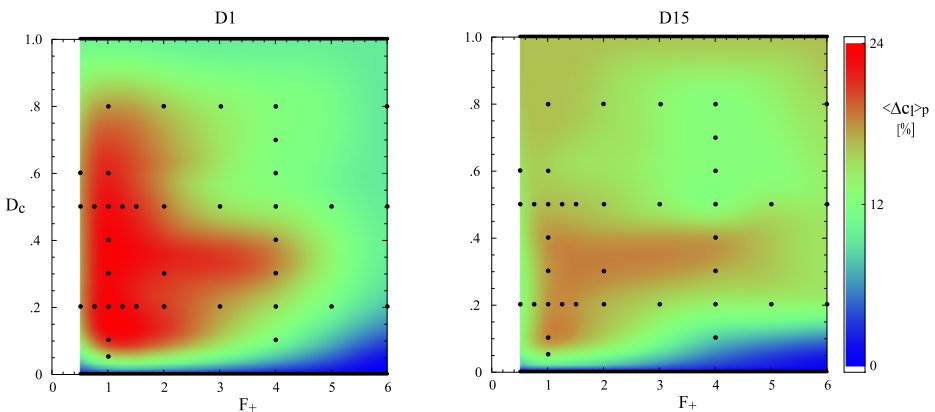


Fig. 13 Maps of $\langle \Delta c_l \rangle_p$ as function of F_+ and D_c for D1 and D15 at $U = 20$ m/s

instead is almost completely determined by the plasma discharge, since $\langle \Delta c_l \rangle_t \simeq \langle \Delta c_l \rangle_p$ or, looking at the least significant digit, the passive effect appears to be slightly detrimental in this case.

The performance of D1 and D15 as function of F_+ and D_c can be visualized as in Fig. 13: for D1 the point $(F_+, D_c) = (1, 0.1)$ belongs to a bounded region of optimal working mainly located around $F_+ = 1$; also for D15 the modulation $F_+ = 1$ is effective, but the performance is good in a larger area of the plane that extends to the steady actuation (top line). The best values of $\langle \Delta c_l \rangle_p$ are obtained here for quite short duty cycles; these results can be compared with the literature data for the same airfoil, for example He et al. obtained a large lift increase in the postcritical range for $F_+ = 1$ and $D_c = 0.1$ at $Re = 307k$ [26], whereas Benard et al. found as best conditions $F_+ = 0.75$ and 1 at $Re = 250k$ with larger duty cycles, up to 0.5 [19, 32]. Operating at a lower Reynolds number ($Re = 63 k$) Sekimoto et al. [33] showed that $F_+ = 1$ is effective for deep stall, whereas much higher F_+ are preferable in early stall, in order to promote turbulent transition.

The comparison of Tables 2 and 3 shows that the improvement of D15 passing from steady to pulsed actuation is not as large as for D1. This can be observed in detail in Fig. 14 that compares steady and pulsed actuation for both DBDs, including the baseline and plasma off curves: for D1 there is a good stall delay turning the actuator steadily on, and with pulsed operation a further large improvement for large α , together with a small decrease in the maximum lift performance. For D15 instead, the steady actuation already gives a large displacement of the c_l curve, whereas the pulsed operation represents only a minor improvement, even if it brings the c_l curve to interesting values up to $\alpha \simeq 25^\circ$. The straight actuator D1 is the object of a wide literature, so that the above results can be interpreted according to several previous studies: the plasma sheet originating from the straight electrode acts by adding streamwise momentum into the boundary layer, and this mechanism becomes intermittent with pulsed actuation. In turn, this modifies the natural vortex shedding driving spanwise-oriented vortex structures [32], resulting in a stall control capability greatly improved when F_+ matches the proper scale of the flow. Similar spanwise vortices were also observed in controlling separated flow past bluff bodies [20]. As regards the multi-tip D15, that far exceeds the other multi-tips, in the final discussion it will be shown that its performance could be related with an optimal generation of streamwise vorticity; however, the moderate improvement obtained with pulsed actuation would require further studies, focused on the flow structures generated by this DBD when operated by an intermittent waveform.

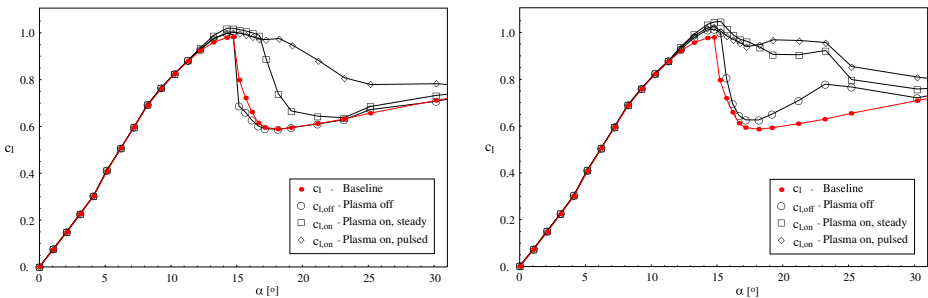


Fig. 14 Lift coefficient vs α for D1 (left) and D15 (right): baseline, plasma off, steady plasma and pulsed plasma with $(F_+, D_c) = (1, 0.1)$

Table 4 Best values of mean drag reduction and working conditions at $U = 20$ m/s

| Actuator | $\langle \Delta c_d \rangle_p, \%$ | $\langle \Delta c_d \rangle_t, \%$ | F_+ | D_c |
|----------|------------------------------------|------------------------------------|-------|-------|
| D15 | 13.6 | 18.8 | 4.0 | 0.8 |
| D1 | 12.1 | 13.5 | 4.0 | 0.6 |
| D14 | 5.4 | 11.5 | | 1.0 |
| D16 | 2.2 | 16.3 | | 1.0 |
| D17 | 2.0 | 15.1 | 4.0 | 0.8 |

The force measurements for the DBD set can be completed by considering their drag reduction capability, estimated here by means of the integral parameters $\langle \Delta c_d \rangle_p$ and $\langle \Delta c_d \rangle_t$ after Eq. 11. These data are presented in Table 4, where the actuators are listed in descending order of relative mean drag reduction $\langle \Delta c_d \rangle_p$. The next columns reports the total drag reduction $\langle \Delta c_d \rangle_t$, and the relevant working conditions (F_+ , D_c). The uncertainty of $\langle \Delta c_d \rangle_p$ and $\langle \Delta c_d \rangle_t$ is in the order of $\pm 0.9\%$.

The largest reduction $\langle \Delta c_d \rangle_p$ in Table 4 is given by D15, with $\langle \Delta c_d \rangle_t$ further increased by the passive effect. Also D1 is very effective, with a smaller passive contribution, whereas the discharge effect is weaker for all the other multi-tips. As a general property, all actuators perform better with high duty cycles and $F_+ = 4$ or with steady actuation; actually, an examination of the $\langle \Delta c_d \rangle_p$ maps on the (F_+ , D_c) domain reveals that a wide range of combined high values of F_+ and D_c is effective for drag reduction, whereas low F_+ and D_c have only weak effects on the drag, and for some actuators the worst regions of the (F_+ , D_c) plane exhibit also a small drag increase. In detail, the performances of the best two actuators as function of F_+ and D_c is presented in Fig. 15, where the properties exposed above are clearly visible, i.e. the optimal region for drag reduction is quite wide for both D1 and D15. The advantages of a high F_+ in this field are mentioned in literature also for a straight actuator on a different airfoil [31], indicating that the best drag reduction is achieved by introducing small flow scales in the boundary layer, whereas the generation of larger structures is more useful for stall control. High F_+ in the order of 20 to 50 were also proved as proper frequencies for the shear layer excitation in a separated flow past an airfoil [17]; however, in the present experiment the attainable F_+ range is lower and values above 20 can only appear in the flow as harmonics of the basic signal.

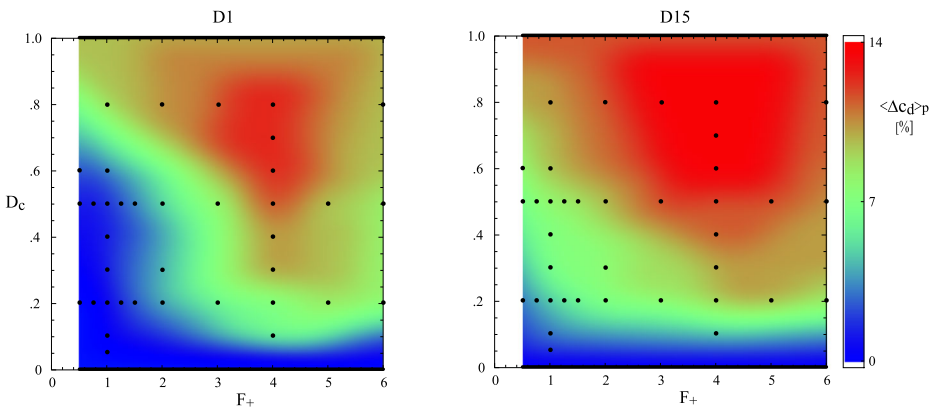


Fig. 15 Maps of $\langle \Delta c_d \rangle_p$ as function of F_+ and D_c for D1 and D15 at $U = 20$ m/s

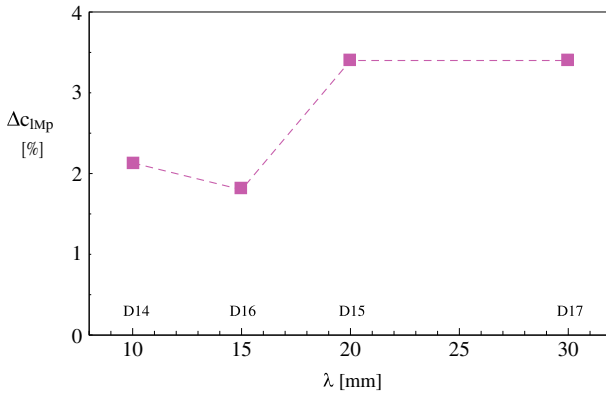


Fig. 16 Maximum lift increases as function of inter-tip spacing λ

As regards the combined effect on lift and drag for D15 and D1, it turns out to be positive: in early stall the optimal (F_+ , D_c) values for maximum lift are also well effective for drag reduction; in deep stall instead, it is not possible to maximize at the same time lift increase and drag reduction, however the optimal point (F_+ , D_c) = (1, 0.1) still gives a small $<\Delta c_{d>p}$ both for D1 and D15.

3.4 Effects of tip spacing

For the electrodes with tips, a better comprehension of the involved physics can be achieved by considering the effects of the inter-tip spacing λ : the actuators under study share the same kind of tip, but with different spacings $\lambda = 10, 15, 20$ and 30 mm for D14, 16, 15 and D17 respectively (the naming does not match the spacing increase because D16 and D17 have been introduced in this work after the initial classification). Since the tips are always $w = 10$ mm wide, the geometry varies from serrated edge (D14) to well separated tips (D17).

As regards the increase in maximum lift, the dependence of Δc_{lmp} on λ is shown in Fig. 16 and reveals an improvement of performance for $\lambda \geq 20$ mm. The impact of tip

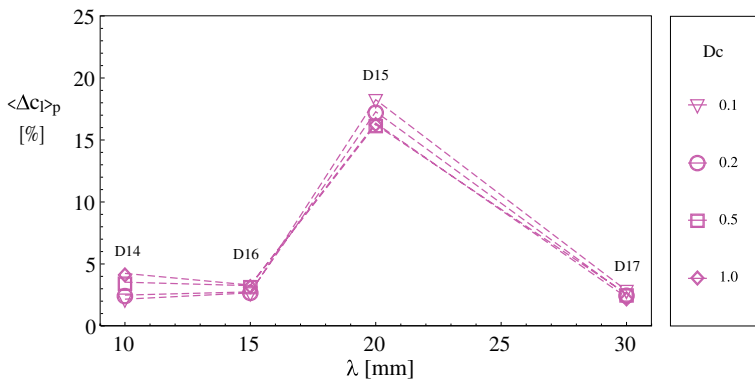


Fig. 17 Mean lift increases vs inter-tip spacing λ , measured at fixed frequency $F_+ = 1$ and several duty cycles

spacing on deep stall performance is visible in Fig. 17, that reports the $\langle \Delta c_l \rangle_p$ values taken at the same frequency $F_+ = 1$ for several duty cycles: here the mean lift increase $\langle \Delta c_l \rangle_p$ has a clear maximum for $\lambda = 20$ mm, indicating the presence of an optimal spacing value (with slightly better values for smaller duty cycles).

The data in Figs. 16 and 17 should be interpreted considering the two working principles of these actuators, streamwise momentum injection and generation of vortices. If momentum injection prevails, assuming this mechanism as essentially determined by the tips effect (considered in detail in Section 3.5), the performance should improve by increasing the number of tips with similar shape, that is with high n and short λ , but this is not verified. An alternative interpretation arises observing that vortex generation between tips is naturally supposed to be dependent on the tip spacing. In fact, a streamwise vortex pair between adjacent tips needs a proper space to develop, as pointed out by Wicks et al. [7]: in their model, the optimal distance λ_{opt} between subsequent elements in a VG is twice the discharge length, also known as plasma length or plasma extent, defined as size of the plasma forming region measured normally to the electrode contour. The plasma length, represented by the width of the shaded band in Fig. 1, is essentially determined by the voltage, always 20 kV_{pp} in this study. Assuming a local reference system in the electrode plane where X is the normal distance from the contour and Y is the coordinate along the electrode contour, the plasma length ΔX has been measured here by means of discharge images, following the method of Kriegseis et al. [23]:

$$\Delta X = X_{\max}[G(X) > G_b] - X_{\min}[G(X) > G_b] \tag{18}$$

where G represents a grey-value image intensity, G_b the background level and the signal is

$$G(X) = \frac{1}{N} \sum_i g(X, Y_i), \tag{19}$$

i.e. a mean value of light intensities $g(X, Y_i)$ measured along several pixel columns Y_i , and acquired over an exposure time of 4 s, much longer than any characteristic time of the discharge. The length ΔX has been measured at first on the straight actuator D1, leading to a linear dependence on the supply voltage, expressed in the range 12 to 20 kV_{pp} by the fit

$$\Delta X = 0.683 + 0.417V_{pp}$$

with ΔX in mm and V_{pp} in kV, with a very small data dispersion (RMS value of residuals = 0.072 mm). The same fit has been obtained by repeating the tests on the straight parts of

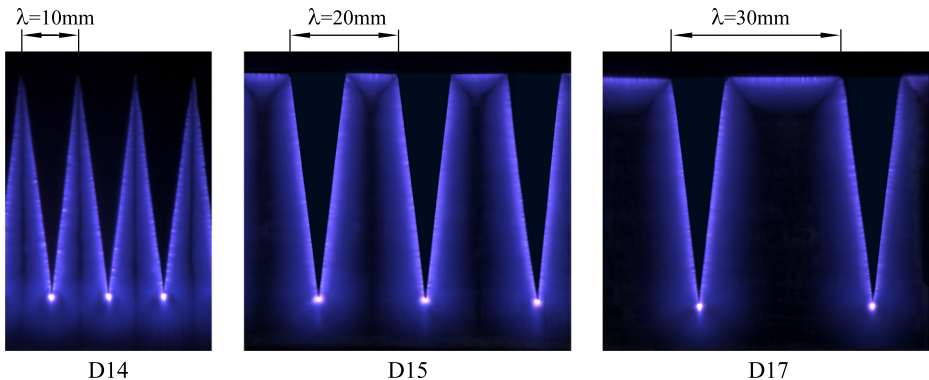


Fig. 18 Discharge patterns for 3 DBDs with different inter-tip spacings

the multi-tip actuators considered in this study, avoiding tips, corners and zones where the discharge extent is bounded by the geometry itself.

The present 20 kV_{pp} voltage gives a length $\Delta X = 9.0$ mm and creates different patterns as λ grows from 10 to 30 mm. This is shown in Fig. 18: for D14 and D16 the discharge cannot develop completely between subsequent tips because $\lambda < 2\Delta X$, the transverse velocity is presumably reduced and the creation of vortices by colliding wall flows is limited. The D15 case with $\lambda = 20$ mm is very close to the optimal distance $\lambda_{opt} = 18$ mm, and for D17 λ is well larger than λ_{opt} , therefore in these two cases the discharge can reach its natural length, allowing the creation of the related vortices without constraints.

According to this interpretation, the early stall performance outlined in Fig. 16 indicates that the highest lift increases are obtained when there is enough space to develop the discharge and the related vortices between tips. Correspondingly, in Table 2 the large λ values of actuators D15 and D17 are associated with large power consumptions W_e/l . This seems to confirm that the mechanism is mainly driven by the physics of the discharge, i.e. all the multi-tips under study with their different geometries create local modifications in the boundary layer, but the better performance of D15 and D17 coincides with their capability of creating full length discharges. In the final discussion it will be shown that for α in the early stall range, even if both these actuators allow the correct discharge development, the vorticity generated by D15 is larger than for D17, owing to their different spacings. As visible in Fig. 16, this property makes no difference for $\alpha \sim \alpha_c$, however in deep stall D17 becomes less effective than D15, as shown in Table 3 for their optimal F_+ and D_c . This behaviour is also confirmed by comparing them under the same operating parameters as in Table 5: the lower vorticity generated by D17 in the post-critical range could give a first explanation for the different trends in Figs. 16 and 17, but further studies are required to support the underlying hypothesis, i.e. that the vortex strength is always determined by the discharge development and the tip spacings, whereas is less affected by the boundary layer thickness and pressure gradients.

3.5 Boundary layer measurements

In order to describe the local flow on the actuators, with particular regard to the stream-wise momentum injection, this section deals with measurements of velocity profiles in the boundary layer. The profiles are acquired by means of a small pitot probe as described in Section 2.3, and the selected points on the airfoil surface are sketched in Fig. 19: two distances s_1 and s_2 downstream of the actuators have been considered as in a previous work [9], namely 17 mm = 0.068 c and 40 mm = 0.16 c from the tips line s_t (for the reference D1 s_t marks the straight line where the plasma is generated, coincident with the leading edge). For each chordwise position, several velocity profiles have been acquired at different

Table 5 Compared values of mean lift increase $\langle \Delta c_d \rangle_p$ for D15 and D17 at $U = 20$ m/s

| | D15 | D17 | F_+ | D_c |
|--|------|-----|-------|-------|
| | 18.3 | 2.9 | 1.0 | 0.1 |
| | 17.2 | 2.5 | 1.0 | 0.2 |
| | 16.2 | 2.6 | 1.0 | 0.5 |
| | 15.2 | 2.2 | 0.5 | 0.2 |
| | 16.8 | 3.4 | 0.5 | 0.5 |

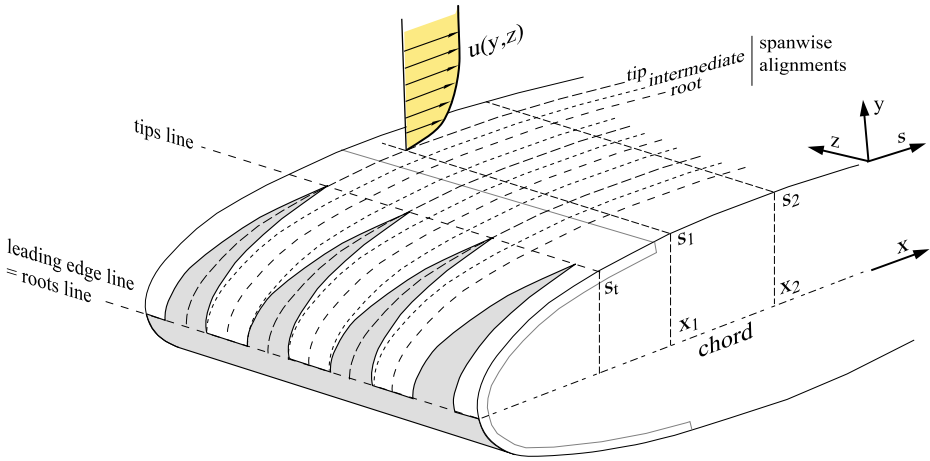


Fig. 19 Boundary layer velocity measurements: selected chordwise and spanwise locations of the probe. The sample velocity profile $u(y, z)$ is not to scale for clarity

spanwise locations, behind tips, roots and intermediate points, in order to obtain local averages as well as spanwise-averaged values. Along each spacing the number of intermediate points ranges from 2 to 4 according to the λ value, i.e. there are 4 to 6 points/spacing. The total spanwise field, explored around the tunnel centerline in order to minimize end effects, is 2.5λ in terms of tips spacing.

These measurements are mainly devoted to assess the maximum control capability of the actuators and help in differentiating the momentum injection from the VG mechanism, so they have been acquired with steady driving ($D_c = 1$). The airstream velocity has been set as above to 20 m/s and the angle of attack to 13° in order to have conditions where the discharge effect is measurable by a pitot probe, downstream of the small recirculating regions described in Section 3.1 for the unpowered actuators and well upstream of the incipient separated flow near the trailing edge. The vortex pairs generated in the inter-tip regions could introduce transversal velocity components on the probe head, however this effect is canceled by symmetry when the probe is aligned downstream of tips and roots, whilst for intermediate points, assuming a crossflow in the order of the ionic wind u_i , an estimation of the misalignment angle due to the crossflow/airspeed ratio gives values smaller than 8° that, accounting for the angular response of the cylindrical pitot head, do not worsen the overall uncertainty.

The velocity profiles can be integrated to determine several quantities of interest: the present analysis will consider the displacement thickness δ^* and the dimensionless momentum coefficient

$$c_\mu = \frac{2}{U^2 c} \int_0^{y_m} (u_{on}^2 - u_{off}^2) dy \tag{20}$$

representing the increase of streamwise momentum due to the actuator, based on the velocity increase u_{on} to u_{off} with the last measurement point y_m lying in the outer flow. The uncertainty of δ^* and c_μ are in the order of $\pm 2.5\%$ of the reported values. Behind an electrode with tips, local information can be retrieved evaluating δ^* and c_μ at different spanwise stations, in particular comparing the values downstream of a tip and a root. Furthermore, δ^* and c_μ vary along the chordwise direction and δ^* can be evaluated with plasma off or on,

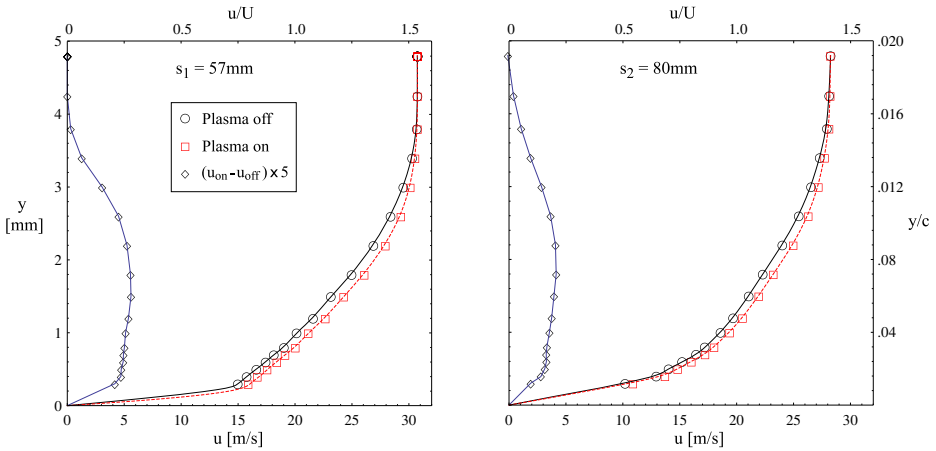


Fig. 20 BL velocity profiles for D15, aligned to a tip at two surface distances s_1, s_2

generating a cumbersome data set. For the sake of brevity, the detailed data analysis will be presented here for D15, considered as a sample multi-tip; afterwards, all the actuators will be compared on the basis of their momentum coefficients.

In Fig. 20, two pairs of on-off velocity profiles downstream of a tip of D15, obtained as mean values of repeated tests, are presented at distances s_1 and s_2 from the DBD. The tips are sources of streamwise oriented wall jets, that increase the local velocity. The corresponding on-off velocity profiles downstream of a root, at the same distances s_1, s_2 , are shown in Fig. 21, and in this case the plasma discharge effect is reversed with respect to the tip region, i.e. the local velocity decreases instead of increasing, as evidenced by the plasma on-off difference trends. This is more visible at position s_1 , closer to the DBD, and for continuity reasons confirms the expected tridimensionality of the flow (vortices between tips).

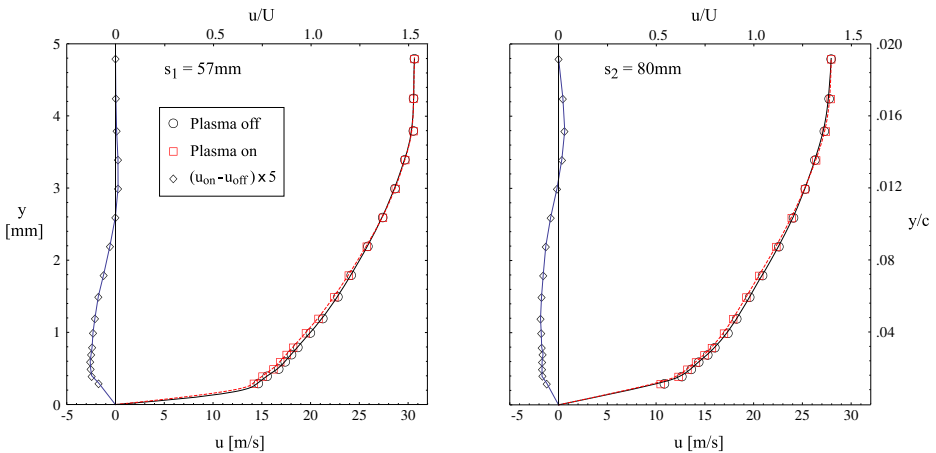


Fig. 21 BL velocity profiles for D15, aligned to a root at two surface distances s_1, s_2

Table 6 Boundary layer displacement thickness δ^* (mm) for D15 at $U = 20$ m/s

| Test condition | Tip | Root | Avg |
|----------------|------|------|------|
| s_1 , off | 0.88 | 0.95 | 0.90 |
| s_1 , on | 0.79 | 0.97 | 0.88 |
| s_2 , off | 0.97 | 1.12 | 1.03 |
| s_2 , on | 0.87 | 1.14 | 1.00 |

The data of Figs. 20 and 21, together with the ones of intermediate alignments, lead to evaluate the actuator impact on the BL thickness δ^* , presented in Table 6. Switching the actuator on, δ_{tip}^* is reduced by plasma effect, whereas δ_{root}^* is increased. For increasing distances (s_1 to s_2), the values are correspondingly larger, but the effects are similar. The table reports also the spanwise-averaged values δ_{avg}^* , obtained by including the data of intermediate alignments, and it can be seen that the plasma effect is a decrease of δ_{avg}^* . All the data in Table 6 intrinsically include the passive effects, due to the 0.12 mm thickness of the active electrode, which is confirmed to be small but not negligible with respect to δ_{on}^* , δ_{off}^* downstream of the DBD. The impact of the electrode thickness can also be regarded with respect to the baseline case (smooth airfoil): for D15, s_1 lies 57 mm from the leading edge, and at the same station in the baseline flow it is found $\delta^* = 0.80$ mm. This value is not very different from the plasma off values at s_1 in Table 6, thus the boundary layer thickness is only slightly modified by the unpowered electrode downstream of the actuator, whereas over the electrode surface there are more significant modifications, as shown in Section 3.1.

The same velocity profiles can be used to evaluate the momentum coefficients for different distances s_1 and s_2 . These data are presented in Table 7, where the capability of D15 as momentum injector is well expressed by the local values behind tips, since they originate streamwise jets. The root values, accordingly to the plots in Figs. 20 and 21, are instead small and negative. The overall effect is represented by the spanwise-averaged values, that include the intermediate alignments data and turn out to be much lower than tips values. As expected, all values decrease for larger distances owing to the momentum consumption along the wall.

Following the same procedure as above, all the actuators under test can be compared in their momentum injection capability by examining their c_μ coefficients, locally behind tips and globally as spanwise averages. These data are collected in Table 8, including the straight electrode of D1. In the tip column the c_μ values are determined by the jets created by the locally high electric field. In particular, c_μ increases with larger spacings. This can be understood by recalling that well separated tips can develop a locally stronger electric gradient, whereas closer tips are expected to give a proportionally smoother electric field. This property has also been evidenced in experiments at the bench [9], and for spacings much smaller than the discharge length the electrode is asymptotically expected to behave as a straight one. The next column reports the spanwise-averaged values, with a completely different trend: here all the values are lower than for D1, since the tips effect is diffused

Table 7 Momentum coefficient c_μ (percentage variation) for D15 at $U = 20$ m/s

| Distance | Tip | Root | Avg |
|----------|------|---------|-------|
| s_1 | 0.28 | − 0.056 | 0.068 |
| s_2 | 0.24 | − 0.047 | 0.054 |

Table 8 Momentum coefficients c_μ (percentage variation) of the DBD set at $s = s_2, U = 20$ m/s

| Actuator | Tip | Avg | λ , mm |
|----------|------|-------|----------------|
| D1 | 0.13 | 0.13 | – |
| D14 | 0.17 | 0.068 | 10 |
| D16 | 0.22 | 0.060 | 15 |
| D15 | 0.24 | 0.054 | 20 |
| D17 | 0.24 | 0.038 | 30 |

over the spacing scale. Moreover, the tips density $n = 1/\lambda$ inherently influences the average values, so that the weaker but numerous jets of D14 lead to a higher average coefficient with respect to the other multi-tips.

The coefficients c_μ have been evaluated with α close to α_c and steady actuation, thus they could be used in interpreting the data of Section 3.3 about early stall performance. However, a model accounting for momentum injection only can not lead to satisfactory conclusions: in fact, a model based on the spanwise-averaged c_μ in Table 8 would indicate a wind tunnel performance improving with a high number of tips, but this is not confirmed by the force measurements. Alternatively, a model accounting for the local c_μ could seem more appropriate, but this automatically implies to consider in detail the spanwise velocity gradient downstream of the actuator, and in turn this leads to examine also the vortex generation mechanism. This is addressed in the final discussion.

4 Discussion

Recalling the data acquired in previous experiments [12, 13] together with the present ones, it is possible to overview the early stall performance of 3 representative actuators as in Fig. 22 over a range of airspeeds extended with further data up to 22.5 m/s. The velocity range is made dimensionless by showing both the Reynolds number and the U/u_i ratio,

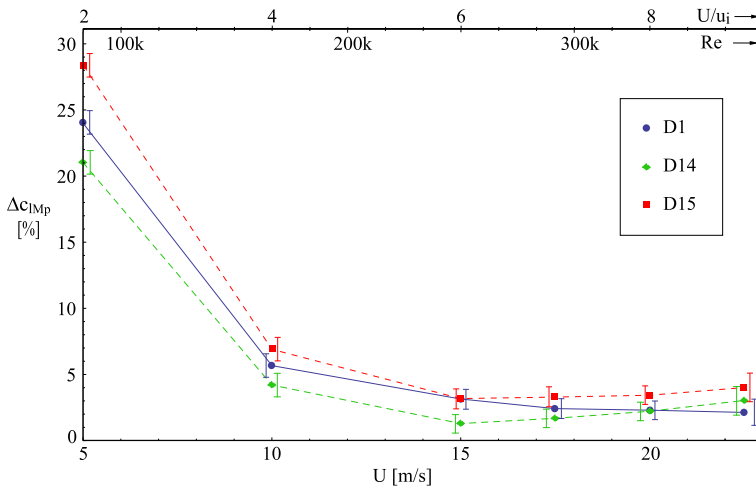


Fig. 22 c_l enhancement in early stall Δc_{lMp} vs airspeed $U, U/u_i$ and Re for 3 representative DBDs

where the airspeed U is referred to the typical ionic wind $u_i = 2.5$ m/s produced by these actuators in still air, as explained in Section 2.1. The figure visualizes the Δc_{lMp} parameter, i.e. the c_l increase due to plasma effect at $\alpha = \alpha_c$, for the straight D1, the serrated edge D14 and the well performant D15, with separated tips. The measured values of Δc_{lMp} are plotted with the relevant error bars, obtained as standard deviations as explained in Section 2.2: although there is a not negligible overlap of the error bars, this comparison indicates a monotonic decrease of Δc_{lMp} for D1, whilst for D14 and D15 the initial decrease is followed by an increase at the highest velocities.

When the fluid is simply accelerated in streamwise direction by a given actuator, the discharge effect can be represented in a simple way by introducing a velocity increase $\Delta u = u_{on} - u_{off}$ in the outer boundary layer at wall distance $y \sim \delta^*$, or at wall in a potential flow model. This can be used to evaluate in turn the circulation enhancement on the airfoil, the lift and the other related quantities. For this mechanism, a decreasing effect for increasing U is commonly expected, so that the generic dependence of Δu on the freestream velocity U can be expressed, asymptotically for large U , as a series of the kind

$$\Delta u = \sum C_n U^{-n} \tag{21}$$

where the maximum allowed order is U^{-1} : in fact, around the airfoil the definition of circulation Γ as closed line integral of the velocity implies that the circulation increase follows the velocity increase, $\Delta \Gamma \sim \Delta u$, and the resulting lift increase according to the Kutta-Joukowski theorem is $\Delta L \sim \rho U \Delta \Gamma \sim \rho U \Delta u$. Therefore, admitting a constant term in series (21) would lead to an unrealistic lift increase growing with U . Assuming instead U^{-1} as highest order, the scaling of velocity increase and lift enhancement takes the form

$$\Delta u \sim a U^{-1} + O(U^{-2}) \tag{22}$$

$$\Delta L_{Mp} \sim \text{const.} + O(U^{-1}) \tag{23}$$

$$\Delta c_{lMp} \sim b U^{-2} + O(U^{-3}) \tag{24}$$

where a, b are constants and the subscript Mp refers as above to the plasma effect under maximum lift conditions. At the first order, the scaling $\Delta c_{lMp} \sim U^{-2}$ has been proposed in literature [34, 35], with the velocity contribution of the actuator corresponding to a doublet field of strength $\sim U^{-1}$. In the large U approximation, the above scaling corresponds also to a decreasing momentum coefficient but a nearly constant magnitude for the difference $(u_{on}^2 - u_{off}^2) \sim c_\mu U^2$, that is both c_μ and Δc_{lMp} scale as U^{-2} . The described asymptotic scaling obviously diverges for $U \rightarrow 0$, however this problem can be solved, improving the model in the low U range, by introducing a shifted variable of kind $U' = U - \text{constant}$. For the straight actuator D1, the scaling described above is compatible with the present dataset and a reasonable fit for Δc_{lMp} can be obtained, as shown in Fig. 23.

On the other hand, this scaling for the multi-tips is unsatisfactory: for the 3 DBDs in Fig. 22, assuming c_l enhancements proportional at $U = 20$ m/s to their average c_μ values (Table 8) and scaling down as U^{-2} to lower velocities would lead to misleading results because i) both the D14 and D15 curves would always be below D1 and ii) all curves would be monotonic. In Figs. 22 and 23 the low velocity data lie in a Re range where the DBDs, besides the circulation enhancement, can give a great improvement to the boundary layer transition. Accordingly, the use of higher order terms could better represent the spread of Δc_{lMp} values at low Re . However, a Δc_{lMp} increase at high airspeeds remains nearly impossible to explain in this way, and makes necessary to consider a different scenario. In what follows, the vortex generation mechanism is assumed as an alternative model.

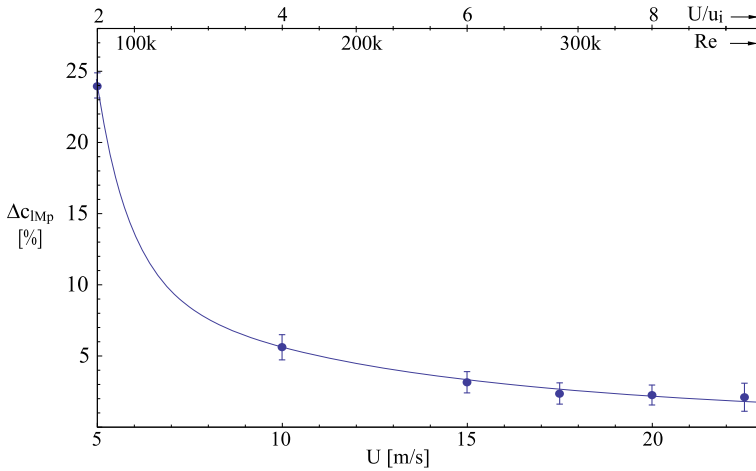


Fig. 23 Early stall c_l enhancement Δc_{lMp} for D1 with U^{-2} fit

As the airstream approaches the actuator, the boundary layer over the leading edge (roots line) has an inherent vorticity ω_z and no streamwise vorticity ω_x ; then, owing to the actuator effect, ω_x develops along the length h of the tips, on a time scale $T_x = h/U_e$ where U_e is the external flow velocity. Referring the physical quantities to $\alpha \simeq \alpha_c$ or larger, over the airspeed range mentioned above, it is easy to verify that the viscous time scale $T_v = \delta^{*2}/\nu$ is much larger than T_x , therefore the streamwise vorticity generation can be estimated by means of the inviscid vorticity transport equation:

$$\frac{D\omega_x}{Dt} = \left(\omega_x \frac{\partial}{\partial x} + \omega_y \frac{\partial}{\partial y} + \omega_z \frac{\partial}{\partial z} \right) u. \tag{25}$$

To perform a simple dimensional analysis, the derivatives can be approximated by finite variations, estimating the vorticity components entering the zone under study at the leading edge (subscript 0), and the velocity derivatives along the tips length h . The dimensional balance is:

$$\frac{\Delta\omega_x}{\Delta t} \approx \omega_{0x} \left(\frac{\Delta u}{\Delta x} \right)_h + \omega_{0y} \left(\frac{\Delta u}{\Delta y} \right)_h + \omega_{0z} \left(\frac{\Delta u}{\Delta z} \right)_h \tag{26}$$

where the temporal derivative is considered in a lagrangian sense, i.e. along a moving fluid particle that in a time interval $\Delta t \sim T_x$ travels a distance in the order of the tip length h . Putting explicitly $\Delta t = T_x$ and recalling that $\omega_{0x}, \omega_{0y} \simeq 0$ at the roots line, Eq. 26 gives:

$$\Delta\omega_x \frac{U_e}{h} \approx \omega_{0z} \left(\frac{\Delta u}{\Delta z} \right)_h. \tag{27}$$

This equation describes the actuators effect as a vorticity realignment $\omega_z \rightarrow \omega_x$, taking advantage of the large spanwise vorticity already present in the approaching boundary layer. The phenomenon represented by Eq. 27 has been also evidenced in detailed studies about streamwise oriented DBDs or PVG [7, 36]. When a fluid element moves over the tip length h , the available time to gain ω_x rotation is set by the time scale T_x , whilst the vortical motion needs a time in the order of $T_r = u_i/\lambda$ to bring a fast fluid element toward the wall. Therefore, this mechanism should work properly when $T_x \sim T_r$ or larger. In a refined model, the vorticity directly added by the actuator could be accounted for by including a

term of kind $\omega_x (\Delta u / \Delta x)$, however it is easy to see that this term is much smaller than the dominant one unless U becomes so low as to be comparable with the ionic wind u_i .

In Eq. 27, the order of magnitude of the spanwise vorticity in the incoming flow is $\omega_{0z} \sim U_e / \delta_0^*$, whilst the gradient $(\Delta u / \Delta z)_h$ can be estimated considering the spanwise variation of streamwise velocity $\Delta u_\lambda = u_{tip} - u_{root}$ induced downstream of the DBD over the half spacing $\lambda/2$, with u_{tip}, u_{root} measured at the representative height δ^* . The present dimensional analysis is based on this simple two-point estimation, however the local gradient can also be checked by means of the intermediate measurements available along a tip spacing (Section 3.5), and it turns out to be of the same order as the linear estimation. Assuming $(\Delta u / \Delta z)_h \sim 2 \Delta u_\lambda / \lambda$, it is obtained

$$\Delta \omega_x \approx \frac{2 \Delta u_\lambda h}{\delta_0^* \lambda}. \tag{28}$$

The streamwise vorticity increase $\Delta \omega_x$ can be estimated after Eq. 28 for a given actuator with tips length h and spacing λ , measuring the velocity differences Δu_λ by the pitot probe as in Section 3.5, whilst the thickness δ_0^* at the leading edge falls below the spatial resolution of the instrument and must be determined numerically: in what follows, this parameter has been estimated by XFOil [28], which is validated by the good agreement with the measurable values in the range s_1 to s_2 over the smooth profile near the centerline (baseline test). Of course, Eq. 28 is a simplified dimensional estimation: for instance, it does not account for the transitional phenomena occurring along the tips length as U changes. However, for any fixed U , it provides a useful tool to the present purpose of comparing multi-tips of similar length h and different spacings λ .

The performance of D14 and D15 in Fig. 22 can now be described as a combined effect of forward momentum added directly by the discharge and momentum taken from the external flow by the vortices. The estimated streamwise vorticity of D14 and D15 is shown in Fig. 24 as function of the airspeed U , including dimensionless values $\Delta \omega_x c / u_i$ referred to the scales c and u_i , constant for the whole experimental campaign, and dimensionless parameter U / u_i and Re for the airspeed. As expected from the discharge length measurements, D15 produces much more $\Delta \omega_x$ than D14, and this vorticity remains fairly high over the whole U range, even if it decreases for low airspeeds. The lift enhancement Δc_{lMP} in Fig. 22 can now be interpreted assuming a momentum injection that loses effectiveness as U^{-2} , whereas the VG mechanism is always present and slowly growing with U , so that above 15 m/s or $U \sim 6 u_i$ it becomes dominant and the lift enhancement becomes mainly sustained by this effect. With the present simplified approach, the agreement between the lift improvements of D14 and D15 and their estimated vorticities is qualitative, and it should be noticed that, while this interpretation may be reasonable to the present data, its possible extrapolation toward higher airspeeds requires a further discussion of the validity conditions, which is done in the final section.

In Eq. 28, $\Delta \omega_x$ depends on the spacing through the gradient $\Delta u_\lambda / \lambda$, where λ acts directly on the denominator and indirectly on the numerator $\Delta u_\lambda = u_{tip} - u_{root}$ by influencing the discharge development and the induced ionic wind. All the actuators tested in this work can be examined by considering the relevant Δu_λ values, leading to a consistent interpretation. In particular, D14 is affected by a low $\Delta u_\lambda = 0.82$ m/s at $U = 20$ m/s, because its short spacing contrasts the discharge development. Instead Δu_λ is 2.8 m/s at the same airspeed for D15, in line with the discharge length analysis in Section 3.4. In the same section, the spacing λ of D16 resulted lower than needed, the correspondingly measured Δu_λ is 0.9 m/s and Eq. 28 gives an estimated $\Delta \omega_x$ less than half of the D15 value. For D17 instead the spacing λ permits a complete discharge development and Δu_λ is 2.3 m/s, comparable to

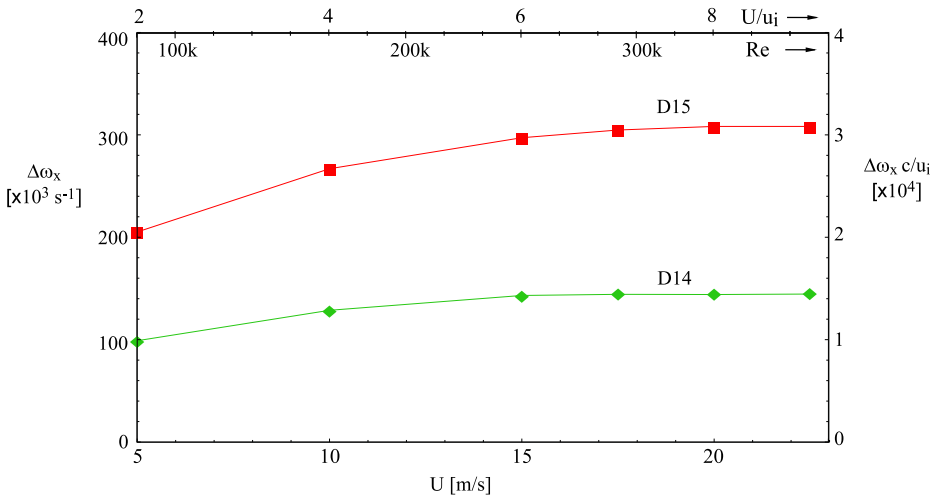


Fig. 24 Estimated streamwise vorticity $\Delta\omega_x$ vs U for D14 and D15, with dimensionless values $\Delta\omega_x c/u_i$, U/u_i and Re

the D15 value, however the large λ reduces the gradient $\Delta u_\lambda/\lambda$, so that even in this case $\Delta\omega_x$ is lower than for D15. The wind tunnel performance of D17 is similar to D15 in early stall and worse in deep stall, suggesting that the vorticity is enough in the former case but not in the latter. As pointed out in Section 3.4, this opens the way to further studies to characterize the flow structures generated by a fully developed discharge in deep stall conditions. Another noteworthy case is the previously studied actuator D5 (serrated edge, $h = w = \lambda = 10$ mm), that was the best out of a large set at $U = 15$ m/s [10]; the available data show that the D5 performance drops at 20 m/s, indicating that the loss of direct momentum is not compensated by a good increase in vortex generation, owing to the low Δu_λ factor (on D5 the discharge can not develop completely) and the low h (short residence time T_x). Finally, in a recent experiment some of the authors have successfully tested a multi-tip DBD on a larger airfoil up to $U = 35$ m/s and $Re = 700$ k [37], designing the actuator accordingly to the model above described, which led in that case to $h = 50$ mm, $w = 10$ mm and a spacing $\lambda = 36$ mm with a higher supply voltage.

All the above data about lift enhancement are compatible with a scaling based on combined terms of kind U^{-n} (momentum injection) and U^β (VG), however this implies a strong hypothesis of linear superposition for the involved mechanisms, which at present is inadequately supported.

5 Conclusions

In summary, considering the present and previous results [9, 12, 13] about separation control by means of multi-tip DBDs, the following conclusions can be drawn. Comparing the airspeed U with the typical ionic wind u_i created by these actuators, in the order of few m/s, the range of interest extends from low airspeeds $U \sim u_i$ to high airspeeds $U \gg u_i$: the streamwise momentum injection due to the tips is mainly effective at low or moderate airspeeds, and the tips sharpness r is not critical, since good results have been achieved with r between 1 and 4. Higher values could presumably perform well, but it is expected a

shorter operating life for very thin tips. The previous experiments indicate that a high tips density n is generally not advisable, since it could weaken the vortex generation. In fact, the streamwise vorticity generation is favoured by properly spaced tips of suitable length, to allow the complete development of the discharge, related to the working voltage. In the proposed scenario, provided that the specific electrode geometry is optimized for the flow to control, the resulting vorticity can give a noteworthy contribution on the whole airspeed range, increasingly important as U/u_i grows.

In designing an actuator, the spacing λ is easily adjustable when using narrow sharp tips, thus the geometry treated in the present work turns out to be a good choice for this kind of DBDs: actually, sharp tips of high r with suitable length h to have a long residence time of the fluid allow the designer to select the right spacing without constraints, and the same tips can work properly even when U/u_i is reduced. The standard serrated shape is not completely excluded by these considerations, but its use is presumably limited to cases where the tips spacing is compatible with the discharge length and the available supply. Finally, in designing an actuator for U/u_i higher than the present ones, the need of a proper residence time T_x imposes to set progressively higher h , that is longer tips, to compare with the available space along the airfoil chord and the boundary layer development. For the same reason, the positive trends of lift enhancement in Fig. 22 for the present airfoil can not be indefinitely extrapolated toward higher airspeeds and even the vorticity estimates in Fig. 24 presumably saturates because h should be longer for larger airspeeds. Similar considerations about scaling the size of the actuators has been done also in other studies applied to ground vehicles [38]. At present the scaling problem is open, and recently an attempt to follow these design rules at larger airspeeds has been done by testing a multi-tip DBD of larger size with encouraging results up to 35 m/s [37].

As regards specifically the detailed tests at $U = 20$ m/s in this work, considering the lift improvement in early stall due to the pure plasma effect, the multi-tips studied in this work perform better than the straight DBD when their spacing is large enough to develop the discharge completely. In the proposed model, this corresponds to an optimized vortex generation, that appears as the most effective mechanism for large velocities. These actuators require more electric power than the straight one, so that their use could be considered a design solution when the available power supply and/or the insulation on the airfoil or wing is limited to a given voltage. In early stall they should operate steadily, whereas in deep stall the pulsed actuation with short duty cycles becomes the best choice: however in this regime the straight DBD remains the best actuator in the present set, and only one multi-tip of optimal geometry can give comparable results. Even in this field the velocity gradient and the relevant vorticity developed downstream of the tips should be important: at present the vorticity generation seems to be mainly related to the availability of space for the discharge development between tips, however the studies should continue by focusing on the flow structures generated by these actuators under different flow regimes. The best multi-tip has proven to be very effective even for the drag reduction purpose, where it can exceed the straight actuator and can also be used to obtain combined lift increase and drag reduction.

In the above description, the discharge effect has been scaled with the airspeed to ionic wind ratio U/u_i to follow the different extents of momentum injection and vortex generation; further considerations must be added when regarding the Reynolds number variation. In general, as recognized in literature, for Re in the order of 100k or lower the capability of the actuators to promote the transition to turbulence is very important. For intermediate Re in the order of 250k the transition enhancement still plays a role, and even in the present tests above 300k the transition, that would naturally take place at a small chord fraction past the leading edge, is favoured by the DBDs. At the same time, in this range the vortex

generation becomes important. For higher Re in the order of 1 million or more, on baseline airfoils with a completely turbulent boundary layer, the actuators are presumably expected to work as manipulators, by vortex generation and/or vortex drivers under pulsed operation.

In this work, the wind tunnel results have been also presented by considering the total effects, i.e. the aerodynamic changes between the smooth airfoil (baseline flow) and the airfoil with a powered actuator, including the passive effects due to the unpowered DBDs. For the actuators under study, the managed power and the need of a reliable operating life led to choose a suitable electrode thickness, small but not negligible with respect to the local boundary layer: at $Re = 330k$, the electrodes interact with the local flow giving passive effects that modify the results, bringing all the multi-tips to exceed the straight DBD in early stall, even for the DBDs that give small off-to-on variations (the visualizations and the measured integral parameters revealed remarkably different passive effects, even in this small set of 5 devices). This suggests to carefully consider the passive effects of the actuators, accounting for the Reynolds number. For electrodes with triangular tips, it is expected that at lower Re the actuators could easily promote the transition to turbulence even when unpowered, whereas for sufficiently larger Re the present results indicate that the passive contribution remains not negligible and the plasma effect becomes large only when the electrode shape is properly optimized. From the designer's point of view, the knowledge of the passive effects can help in foreseeing the global modifications occurring when an active DBD is installed on a smooth body, making the search for a synergy of passive and active effects possible.

Compliance with Ethical Standards

Conflict of interests The authors declare that they have no conflict of interests.

References

1. Forte, M., Jolibois, J., Pons, J., Moreau, E., Touchard, G., Cazalens, M.: Optimization of a dielectric barrier discharge actuator by stationary and non-stationary measurements of the induced flow velocity: application to airflow control. *Exp. Fluids* **43**(6), 917–928 (2007)
2. Thomas, F.O., Corke, T.C., Iqbal, M., Kozlov, A., Schatzman, D.: Optimization of dielectric barrier discharge plasma actuators for active aerodynamic flow control. *AIAA J.* **47**(9), 2169–2178 (2009)
3. Durscher, R., Roy, S.: Induced flow from serpentine plasma actuators acting in quiescent air. In: 49th AIAA Aerospace Sciences Meeting, Orlando, Florida, 4–7 January 2011, AIAA 2011-957 (2011)
4. Wang, C.C., Durscher, R., Roy, S.: Three-dimensional effects of curved plasma actuators in quiescent air. *J. Appl. Phys.* **109**(8), 083305 (2011)
5. Berendt, A., Podliński, J., Mizeraczyk, J.: Comparison of airflow patterns produced by DBD actuators with smooth or saw-like discharge electrode. *Journal of Physics: Conference Series* **301**(1), 012018, 1–4 (2011)
6. Joussot, R., Leroy, A., Weber, R., Rabat, H., Loyer, S., Hong, D.: Plasma morphology and induced airflow characterization of a DBD actuator with serrated electrode. *Journal of Physics D: Applied Physics* **46**(12), 1–12 (2013)
7. Wicks, M., Thomas, F.O., Corke, T.C., Patel, M., Cain, A.B.: Mechanism of vorticity generation in plasma streamwise vortex generators. *AIAA J.* **53**(11), 3404–3413 (2015)
8. Jukes, T.N., Choi, K.S.: Dielectric-barrier-discharge vortex generators: characterisation and optimisation for flow separation control. *Exp. Fluids* **52**(2), 329–345 (2012)
9. Belan, M., Messanelli, F.: Compared ionic wind measurements on multi-tip corona and DBD plasma actuators. *J. Electrostat.* **76**, 278–287 (2015)
10. Messanelli, F., Belan, M.: Ionic wind measurements on multi-tip plasma actuators. *EPJ Web of Conferences* **114**(02073), 1–8 (2016)
11. Belan, M., Messanelli, F.: Wind tunnel testing of multi-tip corona actuators on a symmetric airfoil. *J. Electrostat.* **85**, 23–34 (2017)

12. Messanelli, F., Belan, M.: A comparison between corona and DBD plasma actuators for separation control on an airfoil. In: 55th AIAA Aerospace Sciences Meeting, AIAA SciTech Forum, Grapevine, Texas, 9–13 January 2017, AIAA 2017-0395, pp. 1–14 (2017)
13. Messanelli, F.: Optimization of Plasma Actuators for Flow Control. PhD dissertation, PhD School of Politecnico di Milano. <http://hdl.handle.net/10589/137301> (2018)
14. Vernet, J.A., Örlü, R., Alfredsson, P.H.: Flow separation control behind a cylindrical bump using dielectric-barrier-discharge vortex generator plasma actuators. *J. Fluid Mech.* **835**, 852–879 (2018)
15. Sato, M., Aono, H., Yakeno, A., Nonomura, T., Fujii, K., Okada, K., Asada, K.: Multifactorial effects of operating conditions of dielectric-barrier-discharge plasma actuator on laminar-separated-flow control. *AIAA J.* **53**(9), 2544–2559 (2015)
16. Sato, M., Okada, K., Aono, H., Asada, K., Yakeno, A., Nonomura, T., Fujii, K.: LES of separated-flow controlled by DBD plasma actuator around NACA 0015 over Reynolds number range of $10^4 \times 10^6$. In: 53rd AIAA Aerospace Sciences Meeting, Kissimmee, Florida, January 2015, AIAA 2015-0308 (2015)
17. Aono, H., Kawai, S., Nonomura, T., Sato, M., Fujii, K., Okada, K.: Plasma-actuator burst-mode frequency effects on leading-edge flow-separation control at Reynolds number 2.6×10^5 . *AIAA J.* **55**(11), 3789–3806 (2017)
18. Kelley, C.L., Bowles, P., Cooney, J., He, C., Corke, T.C., Osborne, B., Silkey, J., Zehnle, J.: High Mach number leading-edge flow separation control using AC DBD plasma actuators. In: 50th AIAA Aerospace Sciences Meeting, Nashville, Tennessee, 9–12 January, 2012, AIAA 2012–0906 (2012)
19. Benard, N., Jolibois, J., Moreau, E.: Lift and drag performances of an axisymmetric airfoil controlled by plasma actuator. *J. Electrostat.* **67**(2), 133–139 (2009)
20. Vernet, J.A., Örlü, R., Alfredsson, P.H.: Flow separation control by dielectric barrier discharge plasma actuation via pulsed momentum injection. *AIP Adv.* **8**(075229), 1–19 (2018)
21. Kriegseis, J., Möller, B., Grundmann, S., Tropea, C.: Capacitance and power consumption quantification of dielectric barrier discharge (DBD) plasma actuators. *J. Electrostat.* **69**, 302–312 (2011)
22. Barlow, J.B., Rae, W.H., Pope, A.: *Low-Speed Wind Tunnel Testing*. Wiley, New York (1999)
23. Kriegseis, J., Grundmann, S., Tropea, C.: Power consumption, discharge capacitance and light emission as measures for thrust production of dielectric barrier discharge plasma actuators. *J. Appl. Phys.* **110**(013305), 1–9 (2011)
24. Mabe, J.H., Calkins, F.T., Wesley, B., Wozidlo, R., Taubert, L., Wagnanski, I.: Single dielectric barrier discharge plasma actuators for improved airfoil performance. *J. Aircr.* **46**(3), 847–855 (2009)
25. Melton, L.P., Hannon, J., Yao, C.S., Harris, J.: Active flow control at low Reynolds numbers on a NACA 0015 airfoil. In: 26th Applied Aerodynamics Conference. Number AIAA, vol. 6407 (2008)
26. He, C., Corke, T.C., Patel, M.P.: Plasma flaps and slats: an application of weakly ionized plasma actuators. *J. Aircr.* **46**(3), 864–873 (2009)
27. Komuro, A., Takashima, K., Tanaka, N., Konno, K., Nonomura, T., Kaneko, T., Ando, A., Asai, K.: Multiple control modes of nanosecond-pulse-driven plasma-actuator evaluated by forces, static pressure, and PIV measurements. *Exp. Fluids* **59**(8), 129 (2018)
28. Drela, M., Giles, M.B.: Viscous-Inviscid Analysis of transonic and low Reynolds number airfoils. *AIAA J.* **25**(10), 1347–1355 (1987)
29. Lin, J.C.: Review of research on low-profile vortex generators to control boundary-layer separation. *Prog. Aerosp. Sci.* **38**, 389–420 (2002)
30. Prothin, S., Djeridi, H., Billard, J.Y.: Coherent and turbulent process analysis of the effects of a longitudinal vortex on boundary layer detachment on a naca0015 foil. *J. Fluid Struct.* **47**, 2–20 (2014)
31. Kelley, C.L., Bowles, P.O., Cooney, J., He, C., Corke, T.C., Osborne, B.A., Silkey, J., Zehnle, J.: Leading-edge separation control using alternating-current and nanosecond-pulse plasma actuators. *AIAA J.* **52**(9), 1871–1884 (2014)
32. Benard, N., Braud, P., Jolibois, J., Moreau, E.: Airflow reattachment along a NACA 0015 airfoil by a surface dielectric barrier discharge actuator time-resolved particle image velocimetry investigation. In: 4th Flow Control Conference, Washington, Seattle, 23–26 June, 2008, AIAA 2008–4202
33. Sekimoto, S., Nonomura, T., Fujii, K.: Burst-mode frequency effects of dielectric barrier discharge plasma actuator for separation control. *AIAA J.* **55**(4), 1385–1392 (2017)
34. Hall, K.D., Jumper, E.J., Corke, T.C., McLaughlin, T.E.: Potential flow model of a plasma actuator as a lift enhancement device. *AIAA Paper* **783**, 2005 (2005)
35. Corke, T.C., Mertz, B., Patel, M.P.: Plasma flow control optimized airfoil. *AIAA Paper*, 1208 (2006)
36. Jukes, T.N., Choi, K.-S.: On the formation of streamwise vortices by plasma vortex generators. *J. Fluid Mech.* **733**, 370–393 (2013)

37. Zoppini, G., Di Vinci, L., Campanardi, G., Zanotti, A., Belan, M.: PIV characterization of a separated flow controlled by a DBD actuator. In: XXVI AIVELA National Meeting, J. Phys.: Conf. Ser. 1249–012012 (2019)
38. Vernet, J.A., Örlü, R., Söderblom, D., Elofsson, P., Alfredsson, P.H.: Plasma streamwise vortex generators for flow separation control on trucks. *Flow Turbul. Combust.* **100**, 1101–1109 (2018)

Publisher's Note Springer Nature remains neutral with regard to jurisdictional claims in published maps and institutional affiliations.